Synthesis-Structure-Property Relations in Nanostructured Thin Films Determined by Local Characterization Techniques

Dipl.-Ing. (FH) Angelika Zeilinger

being a thesis in partial fulfillment of the requirements for the degree of a

Doctor of Montanistic Sciences (Dr. mont.)

at the Montanuniversität Leoben

Leoben, August 2014

Financial support by the Austrian Federal Government (in particular from Bundesministerium für Verkehr, Innovation und Technologie and Bundesministerium für Wirtschaft, Familie und Jugend) represented by Österreichische Forschungsförderungsgesellschaft mbH and the Styrian and the Tyrolean Provincial Government, represented by Steirische Wirtschaftsförderungsgesellschaft mbH and Standortagentur Tirol, within the framework of the COMET Funding Programme is gratefully acknowledged.

Affidavit

I declare in lieu of oath, that I wrote this thesis and performed the associated research myself, using only literature cited in this volume.

Leoben, August 2014

Acknowledgments

I would like to express my deep and sincere gratitude to my supervisor Prof. Dr. Christian Mitterer for the possibility to compose my thesis at the Chair of Functional Materials and Material Systems. I would like to thank him for his guidance and support, for his patience in long lasting discussions. His wide knowledge and his mindset have been of great value for me.

I owe my sincere gratitude to Prof. Dr. Keckes for his continuous support, valuable advice and his patience. I also want to thank him for his constructive comments, and for his encouragement throughout this work.

I am deeply grateful to Dr. Rostislav Daniel for his support, his detailed and constructive comments, and for his astute criticism during the writing phase, which helped me to improve my writing style.

I am grateful to the managing directors of the Materials Center Leoben (MCL), for giving me the opportunity to carry out my thesis within an MCL project. I am also thankful to the MCL staff and the co-workers for their support, special thanks go to Bernhard Sartory for his excellent work.

I am grateful to the staff of the synchrotron source Petra III P03 – thank you, Christina, for all your kindness, support and enthusiasm at the beamline.

My special gratitude is due to my colleagues of the “Thin Film Group” at the Chair of Functional Materials and Material Systems and the Chair of Materials Physics for the nice time and unforgettable moments. During this work I have collaborated with many colleagues for whom I have great regard, and I wish to extend my warmest thanks to all those who have helped me with my work, especially to Mario Stefenelli and Juraj Todt – guys you are great!

I owe my loving thanks to my husband and my family and friends, who put up with me for such a long time now. Without their encouragement and understanding it would have been impossible for me to finish this work.

“Don´t drink and scatter!”

by Wulff Morgenthaler

Contents

1. Introduction

Nanostructured thin films grown by plasma-assisted vapor deposition have attracted huge interest due to their outstanding properties, making them suitable for various applications ranging from wear protection to semiconductor devices [1,2,3,4]. Their uniqueness can be attributed to their growth under non-equilibrium deposition conditions, which, however, typically result in an inhomogeneous microstructure in terms of phases and morphology as well as crystallite size, texture and structural defects.

The dominant atomistic processes affecting the microstructural evolution of thin films have been the focus of extensive research in the last decades to generate a basic understanding of the structure formation at the micro-scale. Thus, pioneering and extensive work has been done and the basic relations regarding process-related film microstructure have been comprehensively summarized in structure zone models, which discuss the influence of growth parameters, e.g. deposition temperature, gas pressure, bias potential, on structural film evolution in detail [5,6,7,8].

A prerequisite for the understanding of microstructure evolution has been the development of sophisticated local analysis techniques such as high-resolution transmission electron microscopy. These techniques allow nano-scale characterization of thin films as shown in [9]. Nowadays, with the implementation of cross-sectional X-ray nanodiffraction, new insights into the microstructure of thin nanocrystalline films have been gained, revealing them to be extremely complex regarding crystallographic texture and crystallite size [10]. The technique also allows to determine position-resolved data on the depth gradients [11,12] of residual stresses, which are a consequence of changes in the microstructure evolution during film growth [13].

The microstructure of thin films has been shown to crucially determine their mechanical properties [14]. As thin films are often subjected to severe loading conditions, the establishment of correlations between microstructure and their mechanical properties are of vital importance. However, the establishment of these correlations was up to now a challenging task, as conventional techniques regarding thin film characterization were based on the determination of either surface sensitive or thin film average values. As these correlations are essential for the further improvement of these materials, new techniques enabling position-resolved material characterization have been developed.

Within this work, advanced approaches for characterizing the local microstructure and the residual stress distribution of nanostructured thin films as well as their mechanical properties are presented. Therefore, complex layered thin films with pronounced gradients of microstructure and residual stresses were characterized by ex-situ and in-situ experimental techniques in laboratory and at synchrotron large scale facilities. The techniques were used in order to understand fundamental relations between synthesis, structure and properties of nanostructured thin films and contribute to the basic understanding of the macroscopic behavior of these materials.

2. Nanostructured Thin Films

2.1. Thin Film Synthesis

The synthesis of nanostructured thin films is mainly carried out by physical vapor deposition (PVD) and chemical vapor deposition (CVD) techniques [15]. Both processes are characterized by the formation of a solid product from the reaction in the vapor phase on a substrate material, operating over a wide range of pressures and temperatures. The techniques differ in the state of matter of the material to be deposited and the way of reaction activation. While PVD is based on the transfer of solid material into the gas phase by evaporation or sputtering, in CVD process the deposition of material takes place from a chemical reaction in the vapor phase [16]. The main advantage of the PVD process is the usage of a broad range of suitable materials (metals, alloys, chemical compounds) and the low deposition temperatures. The CVD technique allows the deposition of thin films with high film thickness and is suitable for complex geometries [17].

2.1.1. Physical Vapor Deposition

Physical vapor deposition (PVD) consists of the following three steps : (i) formation of vapor, (ii) its transfer to the substrate material and (iii) subsequent condensation and film growth. PVD can be categorized into sputtering and evaporation, depending on the principle used for transferring the solid material (i.e. target) into the vapor phase [15].

Applying sputter deposition (Fig. 1a), the material is vaporized by bombarding the target surface with energetic ions. Due to energy and momentum transfer atomas are directly ejected of the surface or in a collison cascade, which also results in the ejection of atoms, if the energy of the scattered atoms is high enough. Most of the ejected material are neutrals. An inert working gas (e.g. Ar) is present in the vacuum chamber, which provides the ion bombardment. The ionization of this working gas takes place by applying a voltage between the target (cathode) and the substrate holder (anode), which leads to ignition of a glow discharge (i.e. plasma) [18]. The main advantages of sputter deposition are the smooth film surface and the formation of vapor by momentum transfer, which allows the deposition of materials with high melting points.

Cathodic arc evaporation (Fig. 1b) is characterized by formation of the vapor via an arc discharge (high current, low voltage electrical discharge). It is located between two electrodes in a vacuum chamber, in which the target material acts as the cathode. Thereby the cathode spot (i.e. the area with the highest current density) moves over the target and material is evaporated. The plasma produced at the cathode consists of multiply ionized atoms and is quickly expanding into the vacuum [19,20]. The main advantages of arc evaporation are the high degree of plasma ionization and the possibility to produce very dense thin films. Unfortunately, the process leads to the formation of droplets, i.e. heated and already molten target material, which are incorporated into the growing films. These areas represent defects and lead to a rough surface topography and deteriorates the mechanical properties of the film [21].

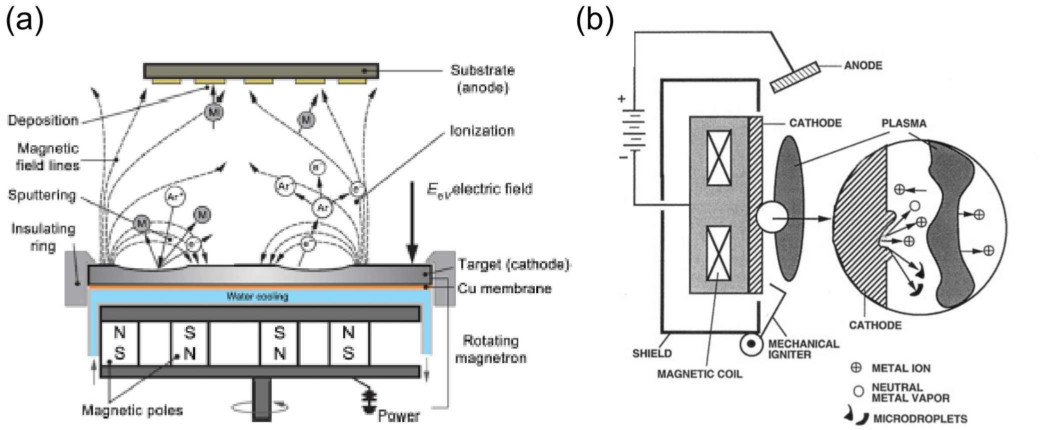

Figure 1*: (a) Illustration of a direct current unbalanced magnetron sputtering system [22] and (b) schematic of the cathodic arc evaporation process with detail of the cathode spot [16].*

2.1.2. Chemical Vapor Deposition

Chemical vapor deposition (CVD) is based on the introduction of gaseous precursor materials into a reaction chamber, which undergo a gas phase reaction and are subsequently deposited on a substrate material [15]. The main reaction steps of the deposition process are illustrated in Figure 2.

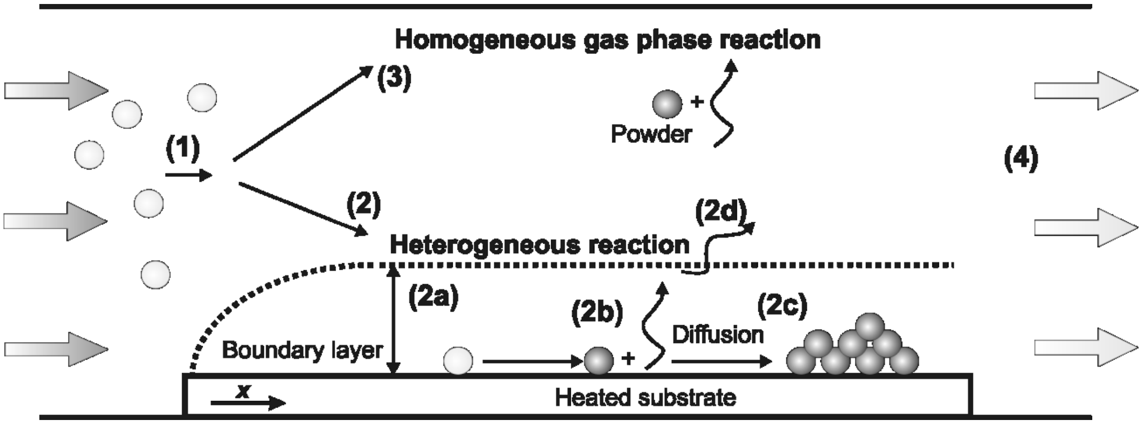

Figure 2: The main steps in the CVD process: (1) Introduction of precursor materials, (2) heterogeneous reaction, (3) homogeneous reaction, (4) gas exhaust. The heterogeneous reaction consists of (2a) the transport of the reactants through the boundary layer and adsorption, (2b) their chemical reaction on the substrate surface, (2c) nucleation and growth, (2d) desorption of by-products. The occurrence of homogeneous gas phase reactions is not favoured. It leads to the production of powder and results in porous films [23,24].

The activation energy for the chemical surface reaction is obtained either by high temperature, laser-assistance or by applying a plasma. The material can be heated by placing the substrate material in a heated furnace or by directly heating the substrate (inductive or resistive heating). The main process parameters are: internal gas stream, velocity and thus the residence time and reactant diffusion to the substrate surface. They can be controlled via the deposition pressure [25,26].

2.2. Thin Film Growth

As soon as vaporized material reaches the substrate, adsorption of the species takes place if its energy is low enough; otherwise the material is reflected by the surface. If the impingment rates are high enough, subsequent atoms adhere at the same spot and small clusters, i.e. nuclei are formed, which can grow by binding of diffusing adatoms or directly by atoms from the vapor phase. The mobility of the species on the surface depends on the following parameters: their kinetic energy, the substrate temperature and the intensity of interactions between species and substrate. After nucleation, growth of the nuclei occurs; they get in contact with each other and coalescence leads to the formation of a continuous layer [27].

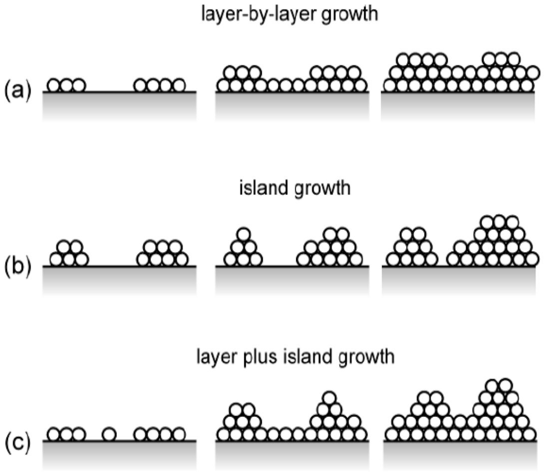

Figure 3: *The three main thin film growth modes: (a) Layer-by-layer, (b) island and (c) mixed layer-island growth [15].*

Three basic growth modes are known and reported in literature (see Figure 3), namely (i) island growth (Volmer-Weber), which typically occurs when the binding energy of the film material is higher than between the substrate material and the film, (ii) layer-by-layer

(Frank-van der Merwe) growth occurs if the opposite is the case, (iii) mixed layer-island (Stranski-Krastanov) growth is a mixture of both modes, where the film starts its growth with monolayers which are superimposed by island growth [16,28].

The deposition parameters have a crucial impact on the nucleation and growth of particles condensing from the vapor phase, which further determine the film microstructure and consequently the mechanical and physical properties of the deposited film. These relationships have been summarized in structure-zone-models (SZM). The first SZM was introduced by Movchan and Demchishin [5], who related the structure of thermally evaporated and sputtered thick films to the homologous temperature T_s/T_m, where T_s is the substrate temperature and T_m the melting point of the film material. In dependence of the thermal activation, they divided their model into three different zones, where in zone 1 the surface mobility is small or close to zero, resulting in porous columnar structure. Surface diffusion processes dominate zone 2, where shadowing effects are overcome and dense films are formed. Bulk diffusion occurs in zone 3, leading to a recrystallized structure. Thornton [6] modified the model by taking into account the most important deposition parameters for PVD processes, namely the total pressure and the ion energy. Thereby a zone called T was introduced, which forms between zones 1 and 2. In zone T, the surface diffusion effect is pronounced and competitive growth occurs, leading to a dense and fibrous structure. Messier et al. [7] modified the SZM by Thornton the following: they introduced the substrate bias potential instead of the inert sputtering gas pressure. An extended SZM has been recently proposed by Anders [29] including the originally proposed three structure zones and the transition zone (Figure 4). There, thin film growth can be categorzied according to the thermal activation temperature (T*), which considers the homologous temperature as well as the additional thermal shift caused by the potential energy of at the film surface arriving particles. T* is plotted as a function of the kinetic activation E*. It describes the displacement and heating effects caused by the kinetic energy of bombarding particles (i.e., atomic scale heating). There is a third axis, which considers the net film thickness t*. It provides to maintain the qualitative illustration of film structure and indicates thickness reduction by densification and sputtering. Also a “negative thickness” is possible in the diagram, due to ion etching at excessive ion energies and intensities. There are two “non-accessible regions”: one at low T* and high E*, as all energy forms arriving at the surface result in a heating of the film and thus, shift the working point to a higher temperature. The second region is situated at very low E*, since the ions coming from the plasma are characterized by a velocity and therefore also a defined energy.

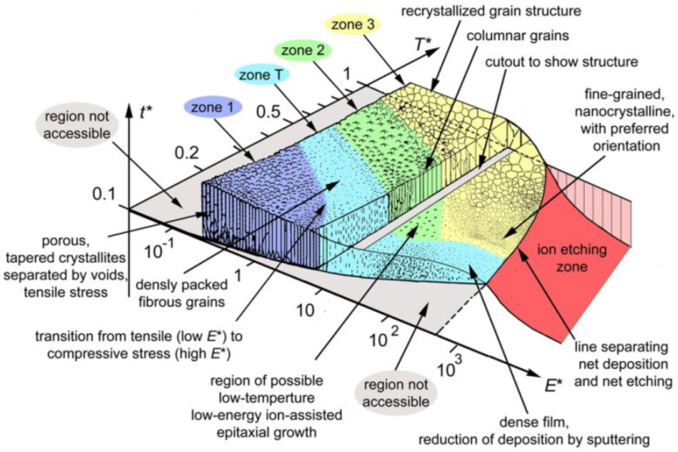

Figure 4: *Recently proposed structure zone model by Anders [29].*

There are three main structures formed during growth of CVD films, which are shown in Fig. 5. In zone 1 the films exhibits columnar crystallites and a smooth surface, which is characteristic for a high deposition temperature resulting in high surface diffusion and uninterrupted crystallite growth. Again a columnar structure can be found in zone 2 but due to lower diffusion and/or higher supersaturation the crystallites evolve more faceted. This leads to a higher film surface roughness. High supersaturation, low temperatures and low pressure lead to the formation of fine equiaxed crystallites as shown in zone 3, a typical phenomenon related to limited diffusion [30].

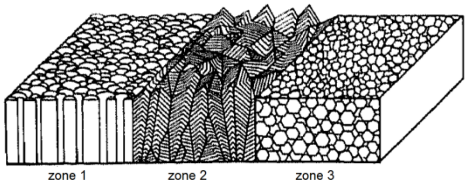

Figure 5: *Structure zone model for thin films deposited by CVD [30].*

2.3 Structural Design and Architecture

Nanostructured thin films mainly consist of transition metal nitrides and carbides in order to improve the properties of tools, mechanical components and electronic devices. These materials can be classified into three groups: covalent, metallic and ionic - based on the dominating chemical bonding character [4,31]. Due to its bonding structure, each material group offers characteristic properties, e.g. high hardness, chemical inertness, good electrical conductivity or excellent wear resistance. As a consequence, a single thin film may not fulfill the requirements for a certain application. Thus, there are several possibilities to further enhance the mechanical properties of nanostructured thin films, which will be explained in the following.

The first approach is to control the microstructure of the film, which invariably defines its mechanical properties. This is realized by adjusting the deposition conditions [9,32,33,34], i.e. deposition temperature, total pressure. The most common way is applying a negative potential (i.e. a bias voltage) to the substrate material, which leads to increased ion energy, resulting in a denser structure and enhanced hardness of the film. This is accompanied by the formation of compressive stresses in the film, which can hinder the initiation of a crack or crack propagation during application [35].

Another approach of thin film improvement is through incorporation and additional elements, e.g. Al, C, Cr. The presence of alloying elements or even a second phase, often causes an improvement in mechanical properties [36,37]. The structure formed can be either crystalline or amorphous [38,39,40]. These material systems are known to exhibit increased hardness, oxidation resistance and impact resistance [41].

Furthermore, besides structural design, thin film architecture plays an important role towards the development of nanostructured thin films with extraordinary properties [42,43,44]. There are various possibilities how the material can be structured, as shown in Figure 6, in order to improve its mechanical properties. According to the shape of the crystallites, which typically exhibit a size of a few nanometers, the materials can be classified into three categories: layer-shaped, rod-shaped and equiaxed crystallites. In the last years layer-shaped architectures have gained much attention, There, the films are composed of periodically varying layers of two or more materials with a typical layer thickness down to 10 nm and up to a few µm. These architectures are characterized by enhanced hardness, moderate residual stresses, improved substrate adhesion. This structures also exhibit enhanced resistance against crack propagation [45,46], which is due to the formation of additional interfaces, interrupting the columnar crystallite growth, and the combination of different materials. If the layer thickness of these structures is in the size of lattice dimensions, superlattice films can be produced. Completely new material properties may be assessed, which are not related to the individual layers [47,48,49,50]. These nanometer scale thin films are devoted to be stable up to high temperatures and therefore phase transformations, crystallite growth or diffusion processes can be retarded [51,52].

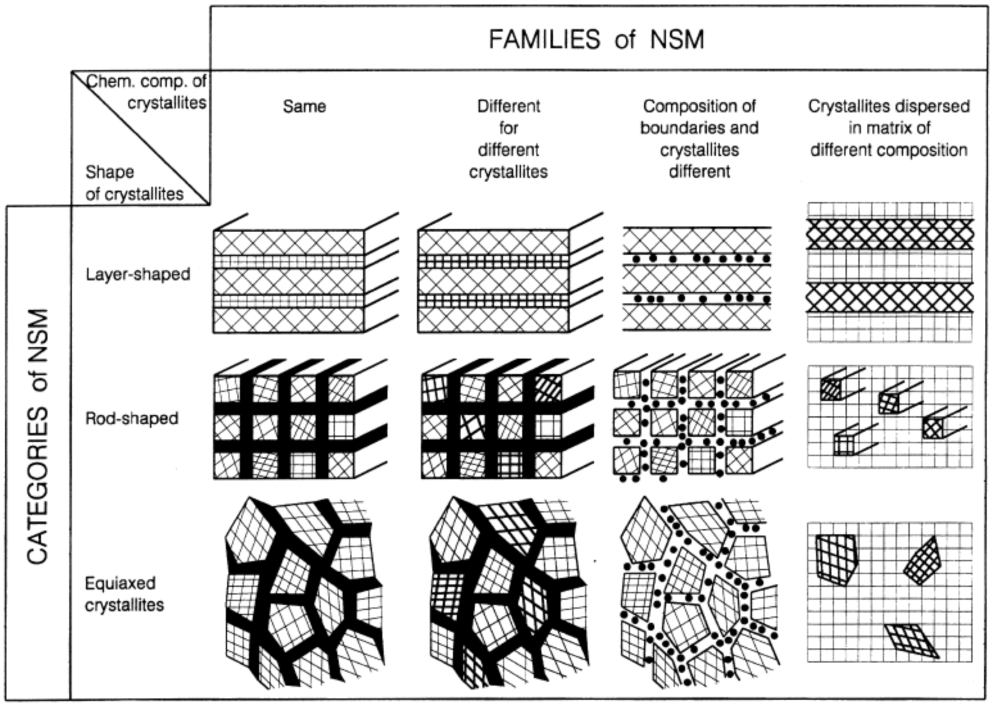

Figure 6: *Classification of nanostructured materials according to their shape of crystallites and chemical composition [42].*

3. Thin Film Characterization

Microstructure as well as mechanical properties of nanostructured thin films were investigated in this work using several approaches and methods. The different experimental techniques are briefly explained in the following chapter.

3.1 Microstructure and Topography

3.1.1. Scanning Electron- and Atomic Force Microscopy

Scanning electron microscopy (SEM) is a standard method used for the investigation of structures at small scale. The principle is based on the usage of an focused energetic electron beam. The interaction of the electron beam with the atoms in the surface area of the sample leads to the production of different signals that can be detected and analyzed. These signals consist of secondary electrons, back scattered electrons and characteristic X-rays, which give information about the sample surface topography and the composition of the material [53,54].

In this work, the morphology of nanostructured thin films was investigated on fracture cross-sections and surfaces using different detectors. Moreover, energy-dispersive X-ray (EDX) spectroscopy (in the SEM) [55,56] was used to identify the chemical composition of the nanostructured thin films on their surface and along the film thickness. Furthermore, SEM was used in order to prepare miniature micro-mechanical samples using a focused ion beam (FIB) technique.

Atomic force microscopy (AFM, also scanning probe microscopy (SPM)), produces topographic images of a surface in 3-D, where a resolution down to about 1 nm can be reached. The setup consists of a cantilever with a sharp Si tip, used for scanning the specimen surface in tapping mode. The tip and the sample interact with each other, which leads to deflection of the cantilever according to Hooke´s law [57]. Depending on the material combination, this can be e.g. mechanical contact forces, van-der-Waals forces, capillary forces, chemical bonding, or electrostatic forces. The deflection of the cantilever tip can be measured by an optical system, where a laser spot is reflected from the top surface of the cantilever. Different modes can be operated using an AFM, depending on the information of interest and the investigated material. In general they include static (also called contact) modes and a variation of dynamic (non-contact or "tapping") modes where the cantilever is vibrated. The tapping mode is similar to the non-contact mode but larger constant vibration amplitudes are used [58,59,60].

In this work, the fracture surface of selected nanostructured thin films was characterized using AFM in tapping mode, according to the procedure described in Publication IV. Furthermore, the technique was used for precise positioning of a diamond tip on bending beams, fabricated for determining fracture properties of thin films, as shown in Publication I.

3.1.2. Scanning X-ray Nanodiffraction

There are several classical experimental techniques available to characterize the local microstructure, i.e. phase evolution, crystallographic texture and crystallite size, in nanostructured thin films, for instance electron microscopy, X-ray diffraction and atom probe tomography [61,62]. One of the main challenges is, however, the necessity of high local resolution without affecting the sample during preparation and/or measurement. Among others, experimental techniques using X-ray photons have seen a rapid development over the last years and the production of highly focused X-ray beams is now possible.

In the field of materials science, scanning diffraction approaches based on position resolved analysis using monochromatic X-ray beams with energy ranges of 5-25 keV and beam sizes down to 100 nm have attracted significant attention [63,64,65,66]. Recently, it has been shown that by the analysis of Debye-Scherer rings it is possible to perform a rapid microstructure and strain/stress characterization of nanostructured thin films. Slices of thin films (with a thickness of about 100 µm) are characterized in transmission mode by scanning across the film thickness. From the full Debye-Scherer rings collected by a 2D detector, local phases, crystallite sizes, texture and residual stresses are determined [10,67,68].

Within the framework of this thesis, this new approach has been applied to analyze nanostructured thin films with defined gradients in microstructure and residual stresses as well as after post-treatment, as shown in Publication II. Furthermore, the data on local microstructure is related to depth-profiling nanoindentation experiments and micro-mechanical tests in order to assess relationships between microstructure and mechanical properties (see Publications III and IV).

3.2. Mechanical Characterization

Indentation is the most applied method for testing the mechanical properties, especially hardness and elastic modulus, of a thin film material. The measurement principle is simple: a diamond tip is pressed into a material of unknown properties. The residual imprint area is then measured and evaluated. Nanoindentation is usually performed by recording the load and the indenter displacement simultaneously during the measurement. The loading curve typically exhibits elastic-plastic behavior, which is followed by an elastic unloading response [69,70]. From this recorded load-displacement curves, hardness and elastic modulus of the film are evaluated according to the method by Oliver and Pharr [71].

Nanoindentation can also be used to characterize mechanical properties of complex thin films with e.g. multi-layer arrangement, variation in microstructure or chemical composition. In order to reveal the local mechanical properties of these films, wedge-shaped depth profiles [72,73] are fabricated by a focused ion beam (FIB) technique on a film/substrate fracture cross-section. Subsequently, the mechanical properties of the film are investigated, by performing nanoindentation experiments at different positions on the wedge (corresponding to different film depths) as shown in Publication III. Although nanoindentation is the most frequently used method for determining local mechanical properties of thin films, no direct information on the stress-strain behavior and orientation-dependent mechanical properties due to their heterogeneous microstructure can be extracted from such studies. There has been extensive work in order to apply miniaturized mechanical tests [74,75] to thin film materials to reveal their elastic-plastic behavior. Nevertheless, the activities often concentrated on the investigation of bulk or amorphous materials at small scale or only on the determination of material specific values [76,77,78]. In this work, a FIB technique was used in order to fabricate miniature samples in the micrometer range from nanostructured thin films. Single- as well as multi-layered thin films were tested by a bending technique and the obtained results were correlated to their apparent microstructures as shown in Publications I and IV.

Nanoindentation is a classical approach in order to analyse local mechanical properties of materials. In the case of nanostructured thin films, the measured mechanical response represents a synergetic value predetermined by microstructure, composition and residual stress state of individual features in the sample. In order to understand and afterwards also to model the indentation response, it is necessary to experimentally characterize microstructural and residual changes in the material occurring *during* the indentation. However, up to now, there have been no in-situ studies of indentation in nanostructured thin films and simultaneous strain measurements. In this work an indentation setup has been designed and implemented to the X-ray nanodiffraction beamline P03 at the Petra III accelerator in Hamburg (see Fig. 7a-c). A notable feature is its fixed indenter tip (with a length of the wedge of 50 µm), positioned on top of the setup frame (see Fig. 7b), attached to a 3 N strain gauge force sensor. The indenter tip was vertically positioned pointing down and initially set to coincide with the nanobeam. The horizontally aligned sample is placed below the indenter tip. Finite element method simulations were employed to obtain a lightweight structure, while ensuring that the applied indentation forces would not lead to a notable deformation of the frame and weaken the precision of the nanoindenter. The diffraction data is recorded using a high resolution 2D CCD detector. The mechanical response, i.e. the strain field, of nanostructured thin films under the acting indenter was measured at different stages of deformation (see Fig. 7d) and the influence of local texture, crystallite size and intrinsic residual stresses are determined.

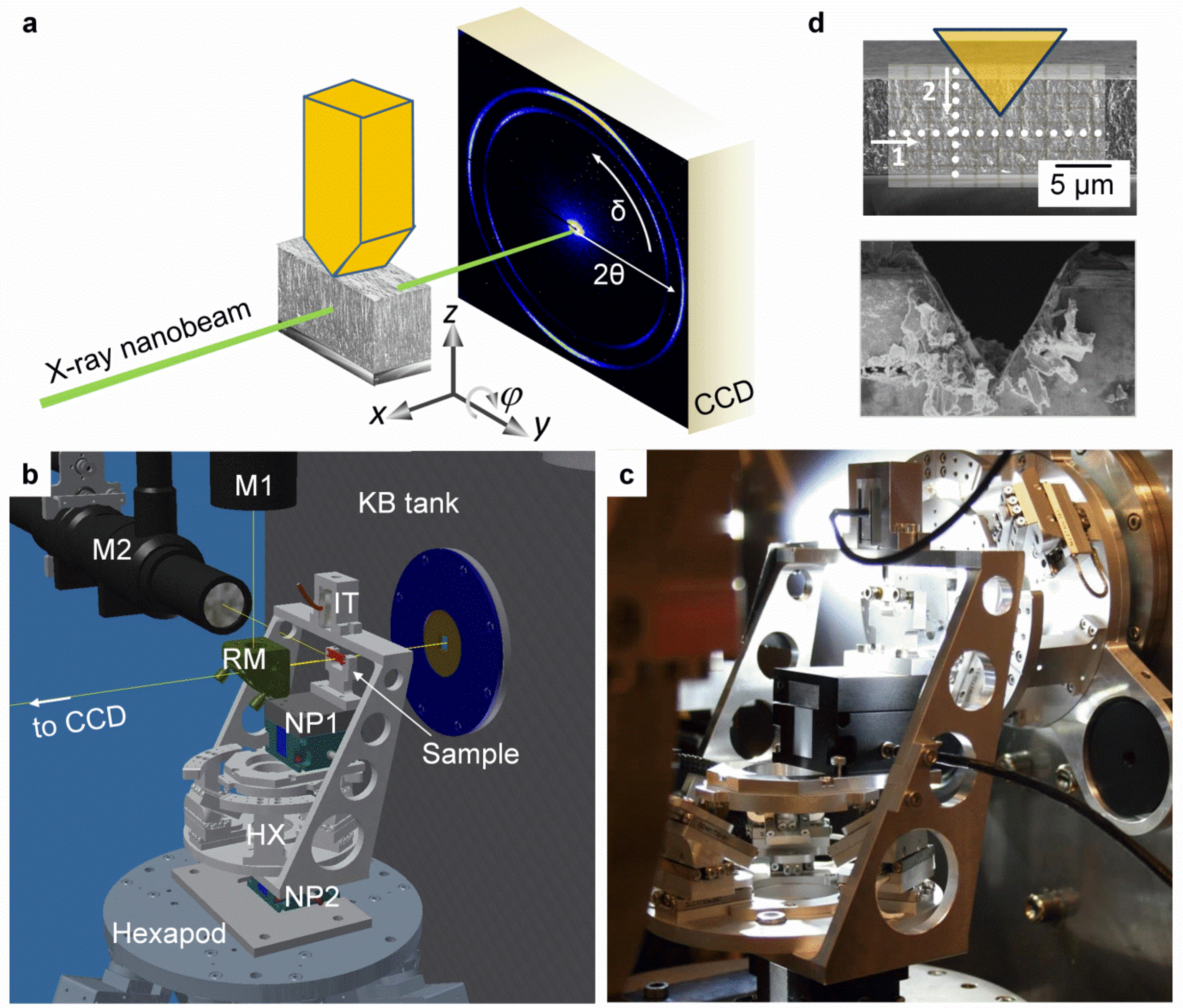

Figure 7: *(a) Schematic view of the position-resolved X-ray nanodiffraction indentation experiment carried out in transmission diffraction geometry. (b) Schematic arrangement of the experimental setup at P03 nanofocus endstation. HX = piezo hexapod, IT = indenter tip and force sensor; M1, M2 = microscopes; NP1, NP2 = piezo nanopositioner, RM = retractable mirror for microscope. (c) Close-up photograph of the indentation setup. The beam direction is from right to left in b and c. (d) SEM image of a thin film sample slice (L = 40 µm) before and after in-situ indentation.*

4. Microstructure-Property Relations

4.1 Hardness and Elastic Modulus

The relationship between the microstructure and the accompanied mechanical properties of nanostructured thin films is of high interest for their understanding and further development. Film hardness is a basic material property and generally measured to characterize a thin film. Primarily the higher the hardness, the higher is the bond strength of the material. Furthermore, the value can be additionally controlled by the thin film microstructure, i.e. the deposition parameters allow tuning of the crystallite size and composition of the material [31,79].

In more detail the bond strength (i.e. the intrinsic hardness) of thin films is a result of the covalent bonds to metallic and ionic bonds ratio [80]. For example, if nitrogen atoms in TiN are replaced by carbon, TiC is formed. The material exhibits a higher amount of covalent bonds and therefore a higher hardness. The hardness of nanostructured thin films can be further enhanced by controlling the crystallite size of the material [81]. According to the Hall-Petch relation [16,82], the hardness of a film increases as its crystallite size decreases. The reason therefore can be attributed to a hindered dislocation movement: during plastic deformation, they have to move across the grain boundaries. These grain boundaries can act as a barrier [83,84], e.g. if the crystallites are differently oriented and if the amount of present grain boundaries increases. Thus, the smaller the crystallite size, the higher is the yield strength which has to be applied for their movement. This hardening effect is present down to crystallite sizes of some 10 nanometers. If the crystallites are too small, an inverse effect is sometimes observed; strength and hardness decrease with decreasing crystallite size [85,86]. It has been shown that the contribution of the crystallite size to the apparent hardness is much higher than other effects, e.g. local texture [88]. The crystallite size of nanostructued thin films can be adjusted down to several nanometers in dependence of the deposition technique and the film material [40]. The preparation of thin films with nanometer sized crystallites is more challenging for CVD then for PVD thin films. The high deposition temperatures in the CVD process often result in coarse columnar growth structures, where the column diameters can be in the micron range [87].

There are other effects which contribute to the increase of hardness in nanostructured thin films. The effect of strain hardening and solid solution hardening are described in refs. [89,90]. Both effects also have in common that the increase in strength is due to restricting or hindering the motion of dislocations in the film. Strain hardening can occur in thin films due to energetic particle bombardment during film growth, which lead to a rearrangement of the lattice. The impinging atoms may also be implanted into the subsurface lattice of the film. If the energy and/or the flux is increased, the number of defects in the lattice increases. Dislocations and lattice defects initiate local strain fields around the lattice disturbance. If a dislocation moves, it requires additional shear stresses to move through the present strain field. As a consequence, a material with a high number of defects appears harder and stronger [14].

If the crystalline thin film matrix is alloyed by other elements, solid solution hardening takes place. If the alloying element is relatively small compared to the size of the matrix atoms, it tends to sit at the interstitial lattice sites. When the atoms are similar in size, the alloying element can sit at the lattice space of the matrix atoms, resulting a substitutional solid solution. The solubility of one element in the crystalline matrix can range from total insolubility to complete solubility. For substitutional solutions it depence on the following parameters: atomic radius, electronegativity and number valence electrons. Solid solution hardening is interpreted as a change of the bonding characteristics as well as alloy interaction combined with dislocation movement [88,89]. Solid solution hardening can be found in several thin film systems. Well-known examples are the $Ti_{1-x}Al_xN$ system [91], but also Ti-Zr-N [92], or Cr-Al-N [93] show this type of hardening mechanism.

Besides hardness, the elastic modulus of thin films can be simultaneously determined using nanoindentation. Due to the non-equilibrium process conditions, its value can – like the hardness - differ completely from those of a bulk material of the same composition and is thus dependent on the deposition conditions during film growth. Using nanoindentation, the received value is interpreted as the isotropic response of the investigated thin film material. However, thin films deposited by CVD or PVD techniques commonly exhibit a strong preferred orientation, which forms due to the different growth modes shown in the previous chapter. Changes in texture significantly influence the elastic modulus of thin films due to material anisotropy. Up to now, investigations according to the orientation dependence of the elastic modulus of nanostructured thin films are at early stage due to a lack of suitable characterization techniques, which allow handling of the small sample size. New approaches concentrate on determining these values by micro-mechanical bending beam tests, which is a promising but time-consuming method.

In this work, the relation between the apparent microstructure and the hardness of nanostructured CrN films have been investigated using X-ray nanodiffraction and nanoindentation wedge-profiling (see Publication III). Furthermore, the elastic modulus of single- as well as multi-layered thin films consisting of Cr and CrN has been investigated by micro-mechanical tests and related to the apparent microstructure and fracture behavior (see Publication IV).

4.2. Residual Stresses

Nanostructured thin films prepared by CVD or PVD techniques typically exhibit a tensile or compressive residual stress state. It is a result of the non-equilibrium process conditions under which the films grow. In general, residual stresses are defined as those stresses that remain in a material after fabrication and processing in the absence of external forces or thermal gradients [94]. The determination of residual stresses in thin nanostructured films can be carried out by the substrate curvature technique. There, the stresses are determined from the curvature of the film-substrate compound, as the compound is bended due to the present biaxial stress generated within the nanostructured thin film. The curvature radius of the composite material is determined by using two parallel laser beams and allows the calculation of the residual biaxial stress using the modified *Stoney* expression [95,96]. Furthermore, residual stresses can be measured by X-ray diffraction using the $\sin^2\psi$ method; further details regarding this measurement technique can be found in [97].

Film stresses can be divided into three categories: (i) thermal, (ii) intrinsic and (iii) extrinsic stresses [98]. Thermal stresses have their origin in the different thermal expansion coefficient of the film and the substrate material, as the films grow at elevated temperature; they are not free to expand or contract when the temperature changes. Their impact to the total residual stress state is mainly dependent on the following parameters: the difference in the thermal expansion coefficients, the deposition temperature and the total film thickness. Thermal stresses are present in the material a long time after the growth process. In comparison intrinsic stresses are generated during film growth. They arise due to the ion irradiation effect of the growing surface, caused by impinging ions of the working gas. In addition, incident particles from the condensing particle flux contribute to intrinsic residual stresses in the material. Generally, compressive stresses are formed due to formation of defects, i.e. interstitials or vacant sites, in the film [99]. Also the volume shrinkage, which goes along with crystallite growth, contributes to the intrinsic stress component by formation of tensile stresses. Microstructure, especially the apparent crystallite size, invariably defines the residual stress state of thin films [99]. Furthermore adatom diffusion to the grain boundaries takes place, which generates compressive stress. Compressive stresses are advantageous in various engineeing applications (e.g. hard protective films for wear applications), as they prevent film failure und thermal and/or mechanical loads. Extrinsic stresses occur due to the following parameters: structural misfit, phase transformation, precipitation, plastic or creep deformation, chemical reactions etc. They have to be taken into account individually in every specific case.

An understanding of the relation between the present microstructure and the accompanied stress development in thin films would enable to further enhance the performance of the nanostructured thin film by controlling the stress level. In this work, experiments on nanostructured thin films, which exhibit a microstructural gradient due to variation in deposition conditions have been carried out. Using X-ray nanodiffraction experiments, the information on the residual stress state and the apparent crystallite size have been related to the phase stability of the different microstructures (see Publication II).

5. Summary and Conclusion

The aim of the present thesis is to contribute towards a fundamental understanding of the relationship between synthesis, structure and properties of nanostructured thin films. This is achieved by the implementation of advanced characterization techniques, which allow the evaluation of microstructure and mechanical properties at the sub-micron scale and with high spatial resolution.

The activities in the field of characterization techniques concentrated on “home” laboratory as well as large scale facility based methods. Applying a cantilever bending technique to nanostructured thin films widened the application field of micromechanical tests to small scale samples with inhomogeneous character. The developed technique allows a reliable determination of values on orientation related elastic modulus, fracture stress and fracture toughness. Furthermore, thin film failure mechanisms are revealed. Scanning X-ray nanodiffraction, using beamlines at the synchrotron sources P03 Petra III / DESY and ID13 at ESRF, provide a new insight into the microstructure of thin films. The suggested technique is a powerful tool for local characterization of phases, texture and crystallite size as well as residual stresses of thin films. Depth-gradients of relations between deposition conditions and resulting microstructure can now be established. In addition, the technique allows investigation of the degradation behavior of nanostructured thin films. Also microstructure gradients in multilayered film compared to the single materials can be investigated.

The new approaches allow a better understanding of the relationship between the structure and the properties of nanostructured thin films as they can be combined with established characterization techniques, i.e. nanoindentation. This allows for example to determine the local relationship between the apparent hardness of a thin film and its microstructure (Publication III).

The now available characterization techniques provide the basis to understand the complex relationship between growth parameters, microstructure and mechanical properties of nanostructured thin films. Thus, they allow to design materials with exceptional performance, made possible by the knowledge of the relation between the local microstructure and the local mechanical properties now. This is a necessary prerequisite in order to understand the macroscopic behavior of nanostructured thin films.

This thesis presents several attempts to establish synthesis-structure-property relationships in nanostructured thin films. However, it also allows pointing out several areas of possible future work. Within this thesis, single- and multi-layered thin films have been characterized by micro-mechanical tests. The technique should also allow the testing of samples with different chemical composition as well as anisotropic properties of thin films. Additionally, the successful implementation of the in-situ indentation technique using synchrotron sources opens a broad research field. The developed techniques allows understanding the outstanding properties of multi-layer architectures and represent therefore powerful tools for the future.

6. References

[1] B. North, Surf. Coat. Technol. 106 (1998) 129.

[2] K. Wetzig, C.M. Schneider, Metal Based Thin Films for Electronics, second ed., Wiley-VCH, Dresden, 2006.

[3] R. Daniel, J. Musil, Novel Nanocomposite Coatings: Advances and Industrial Applications, Pan Stanford Publishing, London, 2014.

[4] A. Cavaleiro, J.Th.M. De Hosson (Eds), Nanostructured Coatings, Springer, New York, 2006.

[5] B.A. Movchan, A.V. Demchishin, Phys. Met. Metallogr. 28 (1969) 653.

[6] J.A. Thornton, J. Vac. Sci. Technol. 11 (1974) 666.

[7] R. Messier, A.P. Giri, R.A. Roy, J. Vac. Sci. Technol. A 2 (1984) 500.

[8] P.B. Barna, M. Adamik, Thin Solid Films 317 (1998) 27.

[9] I. Petrov, L. Hultman, U. Helmersson, J.E. Sundgren, Thin Solid Films 169 (1989) 299.

[10] J. Keckes, M. Bartosik, R. Daniel, C. Mitterer, G. Maier, W. Ecker, J. Vila-Comamala, C. David, S. Schoeder, M. Burghammer, Scripta Mater. 67 (2012) 748.

[11] H. Dölle, J. Appl. Cryst. 12 (1979) 489.

[12] G. Genzel, Phys. Status Solidi A 156 (1996) 353.

[13] R. Daniel, J. Keckes, I. Matko, M. Burghammer, C. Mitterer, Acta Mater. 61 (2013) 6255.

[14] P.H. Mayrhofer, C. Mitterer, H. Clemens, Adv. Eng. Mater. 7 (2005) 1071.

[15] R.F. Bunshah, S.M. Rossnagel, G.E. McGuire (eds.), Handbook of Hard Coatings, Deposition Technologies, Properties and Applications, Noyes Publications, New Jersey, 2001.

[16] M. Ohring, The Materials Science of Thin Films – Deposition and Structure, Academic Press, San Diego, second ed., 2002.

[17] R.A. Haefer, Oberflächen- und Dünnschicht-Technologie, Teil I, Beschichtungen von Oberflächen, Springer Verlag, Berlin, Heidelberg, 1987.

[18] D.L. Smith, Thin-Film Deposition: Principle and Practice, McGraw-Hill, New York, 1995.

[19] R.L. Boxman, D.M. Sanders, P.J. Martin (eds.), Handbook of Vacuum Arc Science and Technology, Noyes Publication, New Jersey, 1995.

[20] D.M. Sanders, A. Anders, Surf. Coat. Technol. 133-134 (2000) 78.

[21] R.L. Boxman, P.J. Martin, D.M. Sanders (eds.), Handbook of Vacuum Arc Science and Technology, Noyes Publication, New Jersey, 1995.

[22] C. Mitterer in: V.K. Sarin, L. Llanes, D. Mari (eds.), Comprehensive Hard Materials, Elsevier, Amsterdam, 2014, pp. 449.

[23] K.E. Spear, Pure Appl. Chem. 54 (1982) 1297.

[24] K.L. Choy, Prog. Mater. Sci. 48 (2003) 57.

[25] J.M. Blocher in: R.F. Bunshah, Deposition Technologies for Films and Coatings, Noyes Publication, Park Ridge, New Jersey, 1982.

[26] D.M. Dobkin, M.K. Zuraw, Principles of Chemical Vapor Deposition, Kluwer Academic Publishers, Dordrecht, 2003.

[27] T.W. Barbee, W.H. Holmes, D.L. Keith, M.K. Pyzyna, G. Ilonca, Thin Solid Films 45 (1977) 591.

[28] J.E. Greene in D.T.J. Hurle (eds.), Handbook of Crystal Growth, Vol 1, Elsevier, Amsterdam, 1993.

[29] A. Anders, Thin Solid Films 518 (2010) 4087.

[30] H.O. Pierson, Handbook of Chemical Vapour Deposition, Noyes Publications, Park Ridge, 1999.

[31] H. Holleck, Metall 43/7 (1989) 614.

[32] I. Petrov, L. Hultman, J.-E. Sundgren, J.E. Greene, J. Vac. Sci. Technol. A 10(2) (1992) 265.

[33] T. Hurkmans, D.B. Lewis, H. Paritong, J.S. Brooks, W.D. Münz, Surf. Coat. Technol. 114 (1999) 52.

[34] I. Petrov, P.B. Barna, L. Hultman, J.E. Greene, J. Vac. Sci. Technol. A 21(5) 2003, 117.

[35] S.J. Bull, D.S. Rickerby, Mat. Res. Soc. Symp. Proc. 188 (1990) 337.

[36] S. Zhang, D. Sun, Y. Fu, H. Du, Surf. Coat. Technol. 167 (2003) 113.

[37] H.A. Jehn, Surf. Coat. Technol. 131 (2000) 433.

[38] S. Veprek, Thin Solid Films 317 (1998) 449.

[39] S. Veprek, J. Vac. Sci. Technol. A17/5 (1999) 2401.

[40] P.H. Mayrhofer, C. Mitterer, L. Hultman, H. Clemens, Prog. Mat. Sci. 51 (2006) 1032.

[41] J. Patscheider, T. Zehnder, M. Diserens, Surf. Coat. Technol. 146-147 (2001) 201.

[42] H. Gleiter, Nanostruct. Mater. 6 (1995).

[43] H. Holleck, V. Schier, Surf. Coat. Technol. 76-77 (1995) 328.

[44] H. Gleiter, Acta Mater. 48 (2000) 1.

[45] K. Holmberg, H. Ronkainen, A. Matthews, Ceramics Int. 26 (2000) 787.

[46] B.M. Clemens, H. Kung, S.A. Barnett, MRS Bull. 24 (2) (1999) 20.

[47] P.C. Yashar, W.D. Sproul, Vacuum 55 (1999) 179.

[48] S. A. Barnett, M. Shinn, Annu. Rev. Mater. Sci. 24 (1994) 481.

[49] P.Eh. Hovsepian, D.B. Lewis, W.-D. Münz, Surf. Coat. Technol. 133-134 (2000) 166.

[50] J. Lin, J.J. Moore, B. Mishra, M. Pinkas, W.D. Sproul, Surf. Coat. Technol. 204 (2009) 936.

[51] C. Donnet, A. Erdemir, Surf. Coat. Technol. 180-181 (2004) 76.

[52] S.A. Barnett, A. Madan, I. Kim, K. Martin, MRS Bull. 28 (3) (2003) 169.

[53] L. Reimer, Scanning Electron Microscopy: Physics of Image Formation and Microanalysis, second ed., Springer, Heidelberg, 1998.

[54] W. Zhou, Z.L. Wang, Scanning microscopy for Nanotechnology, Techniques and Applications, Springer, New York, USA, 2006.

[55] A.J. Garratt-Reed, D.C. Bell, Energy-dispersive X-ray analysis in the Electron Microscope, Bios Scientific Publishers Ltd, Oxford, 2003.

[56] P.J. Goodhew, J. Humphreys, R. Beanland, Electron Microscopy and Analysis, third ed., Taylor & Francis, London, 2001.

[57] C.R. Brundle, C.A. Evans, S. Wilson, Encylopedia of Materials Characterization, Butterworth-Heinemann, Greenwich, 1992.

[58] S.N. Magonov, M.H. Whangbo, Surface Analysis with STM and AFM: Experimental and Theoretical Aspects of Image Analysis, VCH, Weinheim, 1996.

[59] R. Wiesendanger, Scanning Probe Microscopy and Spectroscopy, Methods and Applications, Cambridge University Press, Cambridge, 1998.

[60] E. Meyer, H.J. Hug, R. Bennewitz, Scanning Probe Microscopy, The Lab on a Tip, Springer, Heidelberg, 2004.

[61] D. Brandon, W.D. Kaplan, Microstructural Characterization of Materials, second edition, Wiley, Chicester, 2008.

[62] Y. Leng, Materials Characterization, Introduction to Microscopic and Spectroscopic Methods, second edition, Wiley-VCH, Weinheim, 2013.

[63] C. Riekel, M. Burghammer, R. Davies, IOP Conf. Ser. Mater. Sci. Eng. 14 (2010), 012013.

[64] A. Buffet, A. Rothkirch, R. Dohrmann, V. Korstgens, M. Kashem, J. Perlich, G. Herzog, M. Schwartzkopf, R. Gehrke, P. Muller-Buschbaum, S. Roth, J. Synchrotron Radiat. 19 (2012) 647.

[65] C. Krywka, H. Neubauer, M. Priebe, T. Salditt, J. Keckes, A. Buffet, S. Roth, R. Doehrmann, M. Mueller, J. Appl. Crystallogr. 45 (2012) 85.

[66] C. Krywka, J. Keckes, S. Storm, A. Buffet, S. Roth, T. Döhrmann, M. Müller, J. Phys. Conf. Ser. 425 (2013) 072021.

[67] M. Bartosik, R. Daniel, C. Mitterer, I. Matko, M. Burghammer, P.H. Mayrhofer, J. Keckes, Thin Solid Films 542 (2013) 1.

[68] M. Stefenelli, J. Todt, A. Riedl, W. Ecker, T. Müller, R. Daniel, M. Burghammer, J. Keckes, J. Appl. Crystallogr. 46 (2013) 1378.

[69] A.C. Fischer-Cripps, Nanoindentation, Springer, New York, 2004.

[70] A.C. Fischer-Cripps, Surf. Coat. Technol. 200 (2006) 4153.

[71] W.C. Oliver, G.M. Pharr, J. Mater. Res. 7 (1992) 1564.

[72] S. Ulrich, C. Ziebert, M. Stüber, E. Nold, H. Holleck, M. Göken, E. Schweitzer, P. Schlossmacher, Surf. Coat. Techol. 188-189 (2004) 331.

[73] C. Ziebert, C. Bauer, M. Stüber, S. Ulrich, H. Holleck, Thin Solid Films 482 (2005) 63.

[74] T.P. Weihs, S. Hong, J.C. Bravman, W.D. Nix, J. Mater. Res. 3 (1988) 931.

[75] D. Di Maio, S.G. Roberts, J. Mater. Res. 20 (2005) 299.

[76] C. Motz, T. Schöberl, R. Pippan, Acta Mater. 53 (2005) 4269.

[77] S. Johansson, J.-A. Schweitz, L. Tenerez, J. Tiren, J. Appl. Phys. 83 (1988) 4799.

[78] J.N. Florando, W.D. Nix, J. Mech. Phys. Solids 53 (2005) 619.

[79] H. Holleck, J. Vac. Sci. Technol. A 4 (1986) 2661.

[80] P.J. Burnett, D.S. Rickerby, Thin Solid Films 148 (1987) 51.

[81] W. Schatt, H. Worch, Werkstoffwissenschaft, Wiley-VCH, Weinheim, 2002.

[82] P. Haasen, Physical Metallurgy, Elsevier, Amsterdam, 1996.

[83] W.D. Callister, Materials Science and Engineering - An Introduction, John Wiley, New York, 2003.

[84] R.E. Smallman, R.J. Bishop, Modern Physical Metallurgy & Materials Engineering, Elsevier, Eastbourne, 1999.

[85] E. Arzt, Acta Mat. 46 (1998) 5611.

[86] J. Schiøtz, T. Vegge, F.D. DiTolla, K.W. Jacobson, Phys. Rev. B 60 (1999) 11971.

[87] A. Larsson, S. Ruppi, Thin Solid Films 402 (2002) 203.

[88] R. Daniel, E. Jäger, J. Todt, B. Sartory, C. Mitterer, J. Keckes, J. Appl. Phys. 115 (2014) 203507.

[89] G. Gottstein, Physikalische Grundlagen der Materialkunde, 2. Auflage, Springer, Berlin, 2001.

[90] R.W. Cahn, P. Haasen, Physical Metallurgy, Elsevier, Amsterdam, 1996.

[91] M. Zhou, Y. Makino, M. Nose, K. Nogi, Thin Solid Films 339 (1999) 203.

[92] O. Knotek, W.D. Münz, T. Leyendecker, J. Vac. Sci. Technol., A 5/4 (1987) 2173.

[93] J. Vetter, E. Lugscheider, S.S. Guerreiro, Surf. Coat. Technol. 98/1-3 (1998) 1233.

[94] L. Freund, S. Suresh, Thin Film Materials - Stress, Defect Formation and Surface Evolution, Cambridge University Press, 2003.

[95] G.G. Stoney, Proc. Roy. Soc. Lond. A82 (1909) 172.

[96] J.D. Wilcock, D.S. Campbell, Thin Solid Films 3 (1969) 3.

[97] I.C. Noyan, J.B. Cohen, Residual Stress, Measurement by Diffraction and Interpretation, Springer, New York, 1987.

[98] R. Daniel, K.J. Martinschitz, J. Keckes, C. Mitterer, Acta Mater. 58 (2010) 2621.

[99] H. Oettel, R. Wiedemann. Surf. Coat. Technol. 76-77 (1995) 265.

[100] F. Vaz, P. Machado, L. Rebouta, J.A. Mendes, S. Lanceros-Mendez, L. Cunha, S.M.C. Nascimento, Ph. Goudeau, J.P. Riviere, E. Alves, A. Sidor, Thin Solid Films 420-421 (2002) 421.

7. Publications

7.1. List of Included Publications

I. A Novel Approach for Determining Fracture Toughness of Hard Coatings on the Micrometer Scale

A. Riedl*, R. Daniel, M. Stefenelli, T. Schöberl, O. Kolednik, C. Mitterer, J. Keckes

Scripta Materialia 67 (2012) 708-711.

II. A Combinatorial X-ray Sub-micron Diffraction Study of Microstructure, Residual Stress and Phase Stability in TiAlN Coatings

A. Riedl*, R. Daniel, J. Todt, M. Stefenelli, D. Holec, B. Sartory, C. Krywka, M. Müller, C. Mitterer, J. Keckes

Surface and Coatings Technology (2014), in press.

III. Resolving Depth Evolution of Microstructure and Hardness in Sputtered CrN Film

A. Zeilinger, R. Daniel, T. Schöberl, M. Stefenelli, B. Sartory, J. Keckes, C. Mitterer

Submitted for publication.

IV. Mechanical Property Enhancement in Laminates through Control of Morphology and Crystal Orientation

A. Zeilinger, R. Daniel, M. Stefenelli, B. Sartory, L. Chitu, M. Burghammer, T. Schöberl, O. Kolednik, J. Keckes, C. Mitterer

Submitted for publication.

---

*Riedl was the maiden name of the author before marriage.

7.2. My Contribution to the Included Publications

	Conception and planning	Experiments	Analysis and interpretation	Manuscript preparation
Publication I	100	80	80	90
Publication II	100	95	80	100
Publication III	100	70	95	100
Publication IV	100	80	75	90

Supervision not included!

Publication I

Besides the development of the concept of the publication, my contribution comprised the development of a suitable technique for removing the substrate material on which the film was deposited. Furthermore, thin film characterization reported in the manuscript was done by myself. Thin film deposition was done by co-author Rostislav Daniel, fabrication of the cantilevers was done by Bernhard Sartory. I evaluated all results obtained, developed the structure of the publication and wrote the publication.

Publication II

Again I developed the concept for the publication. My experimental work comprised the measurements at the synchrotron source and the thin film characterization. Furthermore, I evaluated the data supported by co-author Juraj Todt. My contribution includes also the interpretation as well as the writing of the whole publication.

Publication III

I have worked out the concept and carried out the thin film characterization. Furthermore, I developed with co-author Bernhard Sartory a suitable geometry cut by FIB, which enables the determination of hardness of thin films as a function of the film thickness. During the measurements I was supported by co-author Thomas Schöberl. I did the data evaluation, their interpretation and wrote the whole manuscript.

Publication IV

Like for all other papers, I developed also the concept for the publication. Furthermore, I carried out thin film characterization and performed the reported synchrotron experiments. I did the micromechanical characterization, supported by co-author Thomas Schöberl. Co-author Bernhard Sartory fabricated the bending beams. During data evaluation and interpretation I was supervised by co-author Otmar Kolednik. I wrote the publication.

7.3. Publications Related to this Work

I. Tribological Properties of Al_2O_3 Hard Coatings Modified by Mechanical Blasting and Polishing Post-Treatment

A. Riedl*, N. Schalk, C. Czettl, B. Sartory, C. Mitterer

Wear 289 (2012) 9-16.

II. Macroscopic Fracture Behaviour of CrN Hard Coatings Evaluated by X-Ray Diffraction Coupled with Four-Point Bending

M. Stefenelli, A. Riedl*, J. Todt, M. Bartosik, R. Daniel, C. Mitterer, J. Keckes

Materials Science Forum Vols. 768-769 (2014) 272-279.

III. X-ray Analysis of Residual Stress Gradients in TiN Coatings by a Laplace Space Approach and Cross-sectional Nanodiffraction: a Critical Comparison

M. Stefenelli, J. Todt, A. Riedl*, W. Ecker, T. Müller, R. Daniel, M. Burghammer, J. Keckes

Journal of Applied Crystallography 46 (2013) 1378-1385.

IV. Residual Stress Fields across a Wedge-Indented Nanocrystalline CrN/Cr Thin Film Revealed by X-ray Nanodiffraction

M. Stefenelli, R. Daniel, W. Ecker, D. Kiener, J. Todt, A. Riedl*, C. Mitterer, M. Burghammer, J. Keckes

Submitted for publication.

V. In-situ X-ray Nanodiffraction reveals Stress and Microstructure Changes in TiN Thin Film During Indentation (Tentative Titel)

A. Zeilinger, M. Stefenelli, J. Todt, C. Krywka, R. Daniel, C. Mitterer, J. Keckes

Manuscript in preparation.

Publication I

A Novel Approach for Determining Fracture Toughness of Hard Coatings on the Micrometer Scale

A. Riedl, R. Daniel, M. Stefenelli, T. Schöberl, O. Kolednik, C. Mitterer, J. Keckes

Scripta Materialia 67 (2012) 708-711.

A Novel Approach for Determining Fracture Toughness of Hard Coatings on the Micrometer Scale

A. Riedl[a], R. Daniel[b], M. Stefenelli[a], T. Schöberl[c], O. Kolednik[c], C. Mitterer[b], J. Keckes[c]

[a] *Materials Center Leoben Forschung GmbH, Roseggerstraße 12, 8700 Leoben, Austria*

[b] *Department of Physical Metallurgy and Materials Testing, Montanuniversität Leoben, Franz-Josef-Straße 18, 8700 Leoben, Austria*

[c] *Erich Schmid Institute of Materials Science, Austrian Academy of Sciences and Department of Materials Physics, Montanuniversität Leoben, 8700 Leoben, Austria*

Abstract

A novel approach is introduced enabling characterisation of mechanical properties of hard coatings on the microscale. The method is based on bending experiments of chemically etched and focused ion beam shaped free-standing coating micro-cantilevers. The coating itself remains unaffected by the preparation, thus completely preserving its interface to surface features. The determination of fracture toughness, fracture stress and Young´s modulus is demonstrated on as-deposited and annealed sputtered CrN coatings revealing dominant intergranular brittle fracture and annealing-induced grain boundary weakening.

Keywords: Coating; Toughness; Micro-cantilever; Mechanical properties; Nanoindentation

There has been a rapid progress in the design of hard protective coatings with outstanding mechanical properties in recent years. Up-to-date developments allow adjusting coating properties by dedicated microstructure [1] and stress [2] design on the nanometer scale. Advancing the material characterisation to receive representative local coating properties by examination of stand-alone material, as it is common for bulk materials, has thus attracted huge interest. In hard coating applications, where a thin brittle film with a thickness of a few microns deposited on a comparatively soft substrate predetermines the life time, optimization, control and also characterisation of coating fracture toughness turned out to be one of the most challenging tasks [3-5].

Up to now no standard procedure for the determination of fracture toughness of free-standing and fully preserved hard coatings in the micrometer range has been established due to a lack of appropriate sample preparation and handling approaches. Available methods can be subdivided into bending, buckling, indentation, scratching and tensile testing [6-8]. These methods are based on determining the critical applied stress where coating failure occurs, and in almost all of them a coating/substrate compound is tested. This extends to the determination of Young´s modulus and fracture stress, which can presently only be evaluated in the near surface region by nanoindentation experiments. A bending experiment, where a free-standing material is loaded under an external force until fracture, thus appears to be one of the most promising methods for determination of local mechanical properties, especially fracture toughness. The decisive advantage is the concentration of the applied stress within the coating, where no assumptions on the stress transfer into the substrate material have to be made. Despite a number of advantages of bending tests, e.g. a simple test set-up and determination of absolute material property values, the preparation of a free-standing coating and the introduction of a sharp crack represent the key challenges to provide a suitable and reliable technique for determining local mechanical properties of hard coatings.

Based on the established cantilever deflection method [9,10], a new methodological approach is proposed. In contrast to conventional preparation techniques, the method allows testing the mechanical behaviour of a hard coating, including the complete process-related thickness-dependent microstructure and strains of II. and III. order gradients. There, the micro-cantilever contains the complete structural information including nanosized grains at the interfacial area as well as the fully developed columnar structure in the coating surface region [2]. Fabricating a free-standing coating cantilever by focused ion beam (FIB) milling or polishing typically introduces an uncontrolled damage of the coating/substrate interface [11]. The capability of the proposed technique, avoiding this damage, is demonstrated for nanocrystalline CrN hard coatings with various stress states, which is a typical representative coating material exhibiting high abrasion and corrosion resistance [12-15].

The coatings were synthesized by reactive direct current magnetron sputtering on (100)-oriented silicon substrates with a thickness of about 3 µm at a total pressure of 1 Pa in an Ar+N_2 gas mixture (with a nitrogen partial pressure of 0.25 Pa), a target sputtering power of 6 kW applied to a 150 mm diameter Cr target, a substrate temperature of 350 °C and a bias voltage of -40 V. Selected as-deposited coatings were subsequently annealed at 500 °C for 1 h in a high vacuum to reduce the intrinsic stress. X-ray diffraction revealed a (100) texture for the as-deposited CrN coatings with an average crystallite size (i.e., size of coherently diffracting domains) of about 20 nm (for more details see [16]); annealed CrN exhibited weakening in the (100) texture. The coatings were found to be under in-plane biaxial compressive stress of -510 MPa in the deposited state and almost stress-free after the annealing, as determined by the $sin^2\psi$-method (Tab. 1). The intrinsic stresses extrapolated from high-temperature wafer curvature measurements of CrN coated silicon strips were -1085 and -485 MPa for the as-deposited and annealed coatings, respectively. Hardness, H, and reduced Young´s modulus, E, were measured by nanoindentation (Hysitron Triboscope) using a Berkovich tip at an applied load of 12 mN and evaluated by the Oliver & Pharr method [17]. H and E of the as-deposited and annealed coatings were determined to 21.2 ± 0.2 and 295 ± 14 GPa and 17.7 ± 0.1 and 229 ± 8 GPa, respectively.

Preparation of a free-standing coating area without damaging the coating/substrate interface, so that the complete coating structure can be accessed for probing its mechanical behaviour, represents the most critical step in the micro-cantilever preparation. This process can indeed be controlled by an optimized etching procedure: First, the coating surface is scratched with a diamond tip in selected areas to enable interaction of the acid with the underlying silicon substrate. The vicinity of the scratched areas is then etched in a stirred potassium hydroxide (30 wt.%) aqueous solution for 1 h at 60 °C. After chemical etching, the specimens are cleaned in distilled water and ethanol. Due to the chemical inertness of the coating and anisotropic silicon etching, a free-standing coating adhering to a well-structured silicon substrate (with developed {111} facets orientated with 54.7° with respect to (100) oriented surface) are formed (see Fig. 1a). The micro-cantilevers were FIB shaped to beam lengths of 10 µm and beam widths of 2 µm, with the height corresponding to the coating thickness of 3 µm. In order to probe elastic properties as well as fracture toughness of the coatings, two sorts of cantilevers were prepared - the first series being unnotched for evaluating fracture stress and Young´s modulus and the second exhibiting a sharp notch with a depth of 500 nm located 2 µm from the silicon support (see Fig. 1b) for fracture toughness determination. The notch was prepared at low ion beam conditions (5 pA, 30 keV) to ensure a small root radius. Further small material bridges, remaining on both sides of the notch, should support the initialization of a real crack tip to avoid overestimation of the fracture toughness [10]. By this combined etching and FIB technique, a total number of 28 micro-cantilevers were produced. They were subsequently loaded with a sphero-conical indenter (tip radius 850 nm) in a nanoindentation system (Hysitron Triboscope), attached to an atomic force microscope (Digital Instruments 3100), enabling accurate positioning of the tip. The loading rate has been set to 100 µN per second.

Fracture stress σ_F of fabricated bending specimens was evaluated as follows [18]:

$$\sigma_F = 6\frac{Fl}{Bw^2}$$

There, F is the maximum applied load at fracture, l the bending length from the silicon support to the positioning of the indenter, B the cantilever width and w the coating thickness. Young´s modulus E, is calculated from the recorded load-deflection curves of the unnotched cantilevers according to [17]

$$E = \frac{4F}{\delta B} \times \left(\frac{l}{w}\right)^3$$

where δ is the displacement at the applied load F. The observed dominant elastic response during the micro-bending experiments excludes plastic deformation of the material in the contact with the tip and validates the assumption of an ideal brittle material to apply linear-elastic bending theory. Fracture toughness K_{IC} was determined from notched coating micro-cantilevers by [19]

$$K_{IC} = \sigma_F \sqrt{\pi a}\, F\left(\frac{a}{w}\right)$$

where σ_F is the fracture stress. The dimensionless shape factor $F(a/w)$ for the given beam geometry has been derived from [20]

$$F\left(\frac{a}{w}\right) = \sqrt{\frac{2w}{\pi a} tan\left(\frac{\pi a}{2w}\right)} \frac{0.923 + 0.199\left(1 - sin\left(\frac{\pi a}{2w}\right)\right)^4}{cos\left(\frac{\pi a}{2w}\right)}$$

where a denotes the notch depth. The distance between the introduced notch and the silicon support has no effect on the determined K_{IC} value.

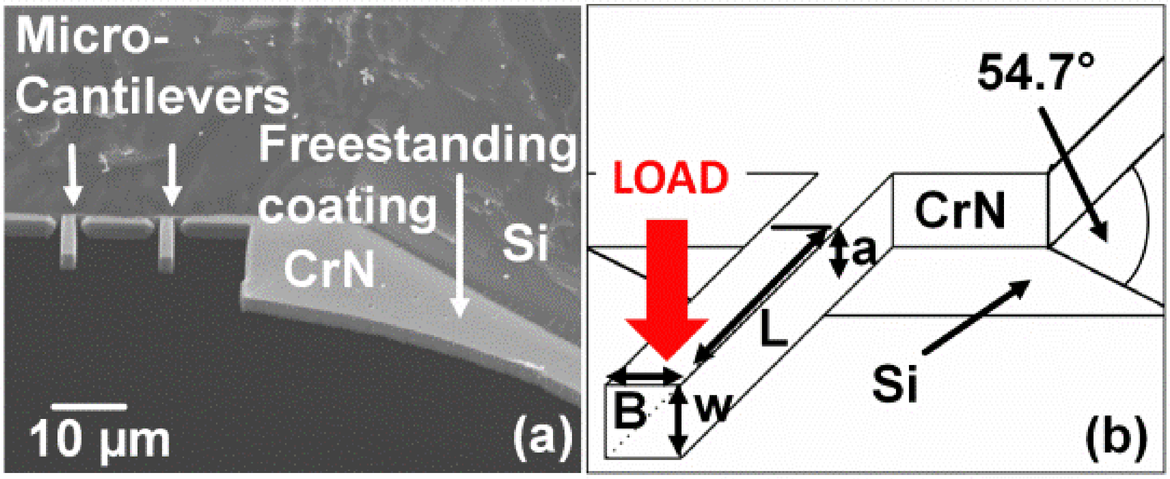

***Fig.** 1: (a) SEM micrograph of a free-standing CrN coating area after etching by potassium hydroxide (bottom-side) and (b) schematic illustration of the cantilever geometry prepared by FIB milling for fracture toughness investigation exhibiting the* *dimensions length, L, width, B, height, w and notch depth, a. A support angle between the coating and substrate material of 54.7 ° is created.*

Micro-cantilever deflection experiments with unnotched specimens revealed a significantly higher fracture stress of the coatings in their as-deposited state (5.86 ± 0.20 GPa) compared to their annealed counterparts (4.43 ± 0.30 GPa) (see Tab. 1). The difference in the mechanical properties of both modifications originates from temperature-induced changes modifying microstructure and intrinsic strain gradients. During annealing above the deposition temperature of 350 °C, the irradiation-induced growth defects [21] in the coating start to recover [22]. Defect annihilation as a diffusion-driven process passes through several stages including defect migration to the grain boundaries (GBs), position exchange of atoms in the lattice and annihilation of vacancies, which may result in a slight grain coarsening despite limited volume diffusion. The compressive stress relaxation together with an atomic rearrangement in the grain interior and at the GBs, affecting their cohesive strength, is subsequently reflected by a change in the mechanical properties of the coatings. The temperature-induced changes thus account for the significant decrease in the fracture stress of the annealed CrN. As revealed by the elastic bending tests of the unnotched micro-cantilevers, the Young´s modulus of 257 ± 27 GPa for the as-deposited coating was reduced to 232 ± 11 GPa by annealing. These values are in a good agreement with the results of the nanoindentation experiments with a Berkovich indenter on the CrN coated silicon substrates. The decrease of about 15 % compared to nanoindentation experiments on the substrate/coating compound is associated with the inherent inhomogeneity of the coating morphology across the coating thickness, originating from competitive character of coating growth [21]. Since the number of GBs increases as the grain size deceases, the effect of GBs representing weakly bonded regions dominates towards the fine-grained coating/substrate interface. Since this effect is restricted by a constraining substrate during a nanoindentation experiment, probing a free-standing film by the deflection method reveals effectively also the weak regions of the coating structure.

Tab. 1: Total, σ_{tot}, and intrinsic, σ_i, stresses, Young's modulus, critical load, F_{max}, and deflection, fracture stress, σ_F, and fracture toughness, K_{IC}, of CrN coatings in the as-

deposited and annealed states as determined from deflection of unnotched and notched cantilevers.

	Coating properties			Cantilevers unnotched			Cantilevers notched		
Coating	σ_{tot} [MPa]	σ_i [MPa]	Young´s modulus [GPa]	Deflection [nm]	F_{max} [µN]	σ_F [GPa]	Deflection [nm]	F_{max} [µN]	K_{IC} [MPa·m$^{1/2}$]
as-deposited	-510 ±54	-1085	257 ±27	574 ±54	1464 ±66	**5.86** ±0.20	345 ±34	1087 ±72	**3.80** ±0.20
annealed	56 ±28	-485	232 ±11	432 ±58	1139 ±88	**4.43** ±0.30	363 ±36	899 ±60	**3.05** ±0.20

Fig. 2 shows load-deflection curves of the notched as-deposited and annealed coatings. The variations in the slopes of the curves have their origin in thermal degradation mechanisms (e.g. stress relaxation, grain growth [1]) initiated by annealing. The critical loads indicated by brittle fracture of the coatings reveal a strong change in mechanical behaviour of the coatings in their as-deposited compared to the annealed state. Despite the lower stiffness of the annealed specimen, the fracture toughness (3.05 ± 0.20 MPa·m$^{1/2}$) is decreased compared to the as-deposited one (3.80 ± 0.20 MPa·m$^{1/2}$). This is in contrast to what is expected and reported for bulk ceramic materials [23]. Fracture toughness of CrN coatings is thus evidently more affected by their complex microstructure than the intrinsic elastic properties of crystallites.

Coating cross-sections and cleavage planes of the fractured coating cantilevers in the as-deposited and annealed states are illuminated by scanning electron microscopy (SEM) in Fig. 3. The fracture surfaces of both specimens show grain scale steps alternating with cavities and hillocks, which are located at the GBs, indicating brittle fracture predominantly occurring along the columnar grains. Although this fracture mode is the same for both specimens, a significant difference in the fracture behaviour is evident (compare Fig. 3c and d). While the as-deposited coating is characterised by macroscopically brittle fracture with limited plasticity corresponding to the ceramic nature of the sample, the cleavage plane of the annealed specimen is evidently more interrupted due to weakened GBs as can be clearly seen in Fig. 3d. Since the cracks initiate at the GBs, the fracture toughness of a brittle nanocrystalline material essentially depends on the cohesive strength of those interfacial areas. The cohesive strength is given by the defect density and impurity content at the GBs, level of nitridation of the GBs and the thickness-dependent microstructural evolution of the coating (as discussed above). Elemental-mappings by energy-dispersive X-ray spectroscopy revealed only slight changes in atom arrangement and no changes in the coating composition before and after annealing, indicating only a minor effect on the fracture behaviour. This excludes nitrogen loss accompanying a possible formation of Cr_2N or the rearrangement of argon atoms at the GBs [24]. More distinct differences in the atom ordering at the GBs, however, can affect the deformation mechanism significantly. Formation of more ordered structure upon annealing followed by the relaxation of compressive stresses, thus generates a network of cracks along the GBs (Fig. 3d) and reduces the shear strength of the interfacial area of the annealed coating. It subsequently promotes abrupt opening of the present cracks, followed by rapid crack propagation under loading across the whole coating thickness, and thus contributes to the catastrophic coating failure.

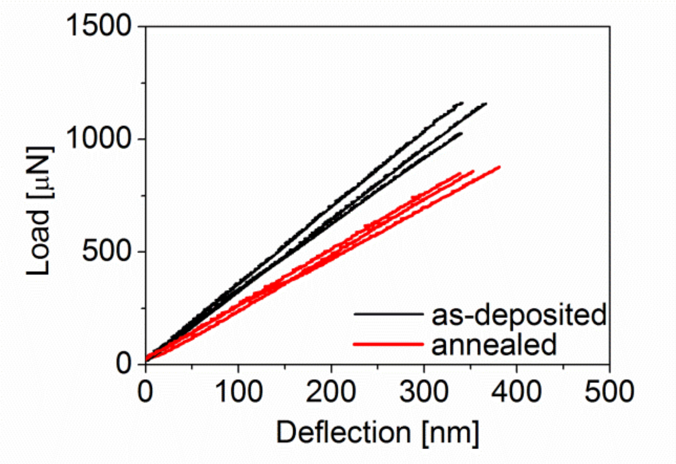

Fig. 2: *Load versus deflection curves of the notched coating micro-cantilevers for fracture toughness evaluation recorded for the as-deposited and annealed CrN coatings investigated. Termination of the load-deflection curves indicates fracture.*

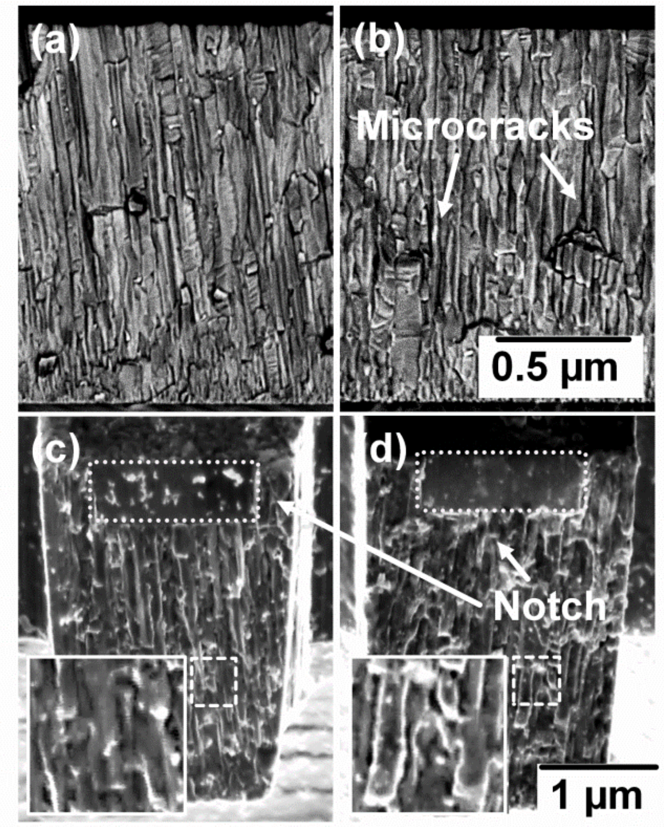

Fig. 3: SEM cross-section micrographs of (a) as-deposited and (b) annealed CrN coatings and cleavage plane of the fractured cantilevers of the (c) as-deposited and (d) annealed modification. The inserts in c and d are 5x magnified.

In conclusion, a novel approach in determining mechanical properties, especially fracture toughness, of free-standing hard coatings by micro-cantilever bending experiments is presented. The technique gains outstanding character by extending the understanding in the design of hard coatings including microstructure and residual stress state by aspects of material behaviour. For the exemplary nanocrystalline CrN hard coatings, the dominating fracture mechanism was shown to be intergranular brittle for the as-deposited as well as for annealed coatings. The decrease in fracture toughness after annealing of the coating is attributed to weakened grain boundaries with reduced cohesive strength, stemming from atomic rearrangement. The presented approach is a powerful tool for providing answers to cutting-edge topics related to coating performance in application and provides insight into coating behaviour in a simple and quick way.

Acknowledgement

Financial support by the Austrian Federal Government (in particular from the Bundesministerium für Verkehr, Innovation und Technologie and the Bundesministerium für Wirtschaft, Familie und Jugend) and the Styrian Provincial Government represented by Österreichische Forschungsförderungsgesellschaft mbH and by Steirische Wirtschaftsförderungsgesellschaft mbH, within the research activities of the K2 Competence Centre on "Integrated Research in Materials, Processing and Product Engineering" operated by the Materials Center Leoben Forschung GmbH in the framework of the Austrian COMET Competence Centre Programme, is gratefully acknowledged.

References

[1] P.H. Mayrhofer, C. Mitterer, L. Hultman, H. Clemens, Prog. Mater. Sci. 51 (2006) 1032.

[2] R. Daniel, K.J. Martinschitz, J. Keckes, C. Mitterer, Acta Mater. 58 (2010) 2621.

[3] G. Jaeger, I. Endler, M. Heilmaier, K. Bartsch, A. Leonhardt, Thin Solid Films 377-378 (2000) 382.

[4] J. Malzbender, G. de With, Surf. Coat. Technol. 135 (2000) 60.

[5] X. Li, B. Bhushan, Thin Solid Films 355-356 (1999) 330.

[6] S. Zhang, D. Sun, Y. Fu, H. Du, Surf. Coat. Technol. 198 (2005) 74.

[7] B.R. Lawn, A.G. Evans, D.B. Marshall, J. Am. Ceram. Soc. 63 (1980) 189.

[8] G.M. Pharr, Mater. Sci. Eng. A 253 (1998) 151.

[9] D. Di Maio, S.G. Roberts, J. Mater. Res. 20/2 (2005) 299.

[10] K. Matoy, H. Schönherr, T. Detzel, T. Schöberl, R. Pippan, C. Motz, G. Dehm, Thin Solid Films 518 (2009) 247.

[11] D. Kiener, C. Motz, M. Rester, M. Jenko, G. Dehm, Mater. Sci. Eng. A 459 (2007) 262.

[12] B. Navinsek, P. Panjan, I. Milosev, Surf. Coat. Technol. 116-119 (1999) 476.

[13] A. Schröer, W. Ensinger, G.K. Wolf, Mater. Sci. Eng. A 140 (1991) 625.

[14] Y.L. Su, S.H. Yao, Z.L. Leu, C.S. Wei, C.T. Wu, Wear 213 (1997) 165.

[15] J.A. Sue, T.P. Chang, Surf. Coat. Technol. 76-77 (1995) 61.

[16] R. Daniel, K.J. Martinschitz, J. Keckes, C. Mitterer, J. Phys. D: Appl. Phys. 42 (2009) 13.

[17] W.C. Oliver, G.M. Pharr, J. Mater. Res. 7 (1992) 1564.

[18] J.M. Gere, B.J. Goodno, Mechanics of Materials, eighth ed., Cengage Learning Emea, Stamford, 2012.

[19] T.H. Courtney, Mechanical Behavior of Materials, McGraw-Hill, Boston, 2000.

[20] H. Tada, P.C. Paris, G.R. Irwin, The Stress Analysis of Cracks Handbook, third ed., ASME, New York, 2000, pp. 55-56.

[21] I. Petrov, P.B. Barna, L. Hultman, J.E. Greene, J. Vac. Sci. Technol., A 21 (2003) 117.

[22] K.J. Martinschitz, R. Daniel, C. Mitterer, J. Keckes, Thin Solid Films 516 (2008) 1972.

[23] B. Lawn, Fracture of Brittle Solids, second ed., Cambridge University Press, Cambridge, 1993.

[24] L. Hultman, J.E. Sundgren, L.C. Markert, J.E. Greene, J. Vac. Sci. Technol. A7 (1989) 1187.

Publication II

A Combinatorial X-ray Sub-micron Diffraction Study of Microstructure, Residual Stress and Phase Stability in TiAlN Coatings

A. Riedl, R. Daniel, J. Todt, M. Stefenelli, D. Holec, B. Sartory, C. Krywka, M. Müller, C. Mitterer, J. Keckes

Surface and Coatings Technology, in press.

A Combinatorial X-ray Sub-micron Diffraction Study of Microstructure, Residual Stress and Phase Stability in TiAlN Coatings

A. Riedl[a], R. Daniel[b], J. Todt[c], M. Stefenelli[a], D. Holec[b], B. Sartory[a], C. Krywka[d], M. Müller[d], C. Mitterer[b] and J. Keckes[c]

[a] *Materials Center Leoben Forschung GmbH, Roseggerstrasse 12, 8700 Leoben, Austria*

[b] *Department of Physical Metallurgy and Materials Testing, Montanuniversität Leoben, Franz-Josef-Strasse 18, 8700 Leoben, Austria*

[c] *Erich Schmid Institute of Materials Science, Austrian Academy of Sciences and Department of Materials Physics, Jahnstrasse 12, Montanuniversität Leoben, 8700 Leoben, Austria*

[d] *Helmholtz Zentrum Geesthacht, Max-Planck-Stasse 1, 21502 Geesthacht, Germany and Ruprecht Haensel Laboratory, University of Kiel, Leibnizstrasse 19, D-24098 Kiel, Germany*

Abstract

The understanding of the relationship between structure and properties of thin coatings is one of the key requirements for their further improvement. Especially for metastable TiAlN, commonly used as a protective coating for cutting applications, detailed knowledge about the apparent microstructure, the resulting residual stresses and the accompanied decomposition behavior at elevated temperatures are of vital importance, as the subsequent high-temperature formation of the thermally stable wurtzite phase results in deteriorated mechanical properties. In this study, the recently introduced cross-sectional scanning X-ray diffraction method is applied as a combinatorial tool to investigate the depth evolution of the local microstructure and residual stresses and their effect on phase stability of a TiAlN coating synthesized by cathodic arc evaporation at stepwise increased bias voltages. The decomposition behavior of the coating during annealing is obviously given by the initial microstructure and stress state, which control the local stress relaxation as well as the formation of precipitates. Thus, the phase transformation is favored in the coating regions that developed under moderate ion-irradiation conditions, characterized by low stress and well-developed columnar grains, and retarded under the presence of high compressive stress. The observed non-linear dependency of phase decomposition on the initial microstructure and stress is interpreted by *ab initio* calculations.

Keywords: Scanning X-ray diffraction; Phase transformation; Residual Stress; Microstructure; TiAlN; Mechanical properties;

1. Introduction

Hard nanocrystalline coatings commonly exhibit complex microstructures across their thickness due to inherently varying growth conditions, self-organization phenomena and/or post-deposition mechanical and thermal loads caused, e.g. by friction between coating and counterpart [1,2,3]. The variation of the coating microstructure is usually accompanied by a depth-dependent variation of the residual stress [4,5,6]. However, the determination of stress gradients as well as the relationship between local variations of microstructure, mechanical and other physical properties is not trivial. This is due to the lack of reliable experimental techniques with sub-micron resolution, enabling to reveal sub-thickness coating properties. Without understanding the microstructure-related physical and functional properties of gradient coatings it is difficult to optimize their performance and prolong their life-time in operation, especially under extreme mechanical and thermal loads. Conventional analytical methods cannot be applied to assess local properties of thin coatings over their complete thickness with sufficient resolution, and thus more advanced techniques are needed.

Cross-sectional scanning X-ray diffraction, using beam sizes down to 50 nm, can provide representative position-resolved data on the depth-evolution of phases, crystallographic texture, crystallite size and residual stresses in thin coatings [4,5]. This technique can also serve as a unique tool for combinatorial investigations, where a variation of deposition conditions can be correlated with the observed variation of the apparent coating microstructure, residual stresses and the environmental behavior of the coating. This is useful especially in the case of complex heterogeneous nanostructured materials.

A representative of such materials is metastable cubic (c) TiAlN, which attracts a significant interest for industrial applications among other transition metal nitrides because of its extraordinary properties at elevated temperatures such as high hardness and oxidation resistance [7,8]. In the last decades, extensive studies on c-TiAlN coatings grown by arc evaporation or magnetron sputtering have been reported, where their microstructure, mechanical properties and residual stresses as well as their high temperature behavior have been investigated [9,10,11,12]. Annealing was found to result in spinodal decomposition of the supersaturated c-TiAlN solid solution into domains of c Ti(Al)N (i.e. TiN where some of the Ti atoms are still substituted by Al) and c-Al(Ti)N (i.e. AlN where some of the Al atoms are replaced by Ti) [13]. Spinodal decomposition was shown to be accompanied by the formation of coherency strains [14] and besides microstructure is also influenced by the intrinsic lattice strains [15]. During further thermal treatment, the metastable c-Al(Ti)N transforms into stable wurtzite (w) AlN [8], which is reported to deteriorate the mechanical properties of the coating [10]. Furthermore, ab initio calculations contributed to understanding the decomposition thermodynamics [16,17].

Thermal treatment results in significant residual stress changes in TiAlN coatings. The usually compressive residual stress in as-deposited TiAlN coatings on Si(100) or WC-Co substrates changes thermo-elastically upon annealing below deposition temperature, subsequently decreases due to the structure recovery above the deposition temperature, increases significantly above the temperature of spinodal decomposition and again decreases during the formation of w-AlN [18,19]. Though there have been significant efforts to assess volume-averaged as well as local properties of polycrystalline as-deposited and annealed c-TiAlN coatings, the full picture of microstructure and strain distribution across their whole thickness, and its effect on decomposition behavior has not been assessed yet.

This study reports on an investigation of microstructure, residual stresses and phase stability of a gradient c-TiAlN coating grown under stepwise increased ion irradiation and investigated in as-deposited state and after annealing at 950 and 1050 °C using a monochromatic X-ray beam with dimensions of 300 × 1500 nm^2. The aims are (i) to relate the actual microstructure and residual stresses of the coatings with the respective ion irradiation conditions and (ii) to elucidate its effect on the decomposition behavior.

2. Materials and Methods

Polycrystalline ~15 µm thick $Ti_{0.54}Al_{0.46}N$ coatings were grown by cathodic arc evaporation onto polished cemented carbide substrates (WC-Co) mounted on a substrate holder located 20 cm from the cathodes in an industrial scale coating system (Oerlikon Balzers INNOVA) using four Ti/Al (50/50) compound targets. The substrate temperature was set to 350 °C, the cathode current was 200 A and the N_2 pressure was 3.2 Pa. A gradient of microstructure and residual stresses in the coatings was achieved by a step-wise increase of the bias voltage during deposition from -40 to -120 V in 20 V steps.

The microstructure of the coating cross-sections was investigated using a Zeiss LEO 1525 scanning electron microscope (SEM). The elemental composition was examined by energy dispersive X-ray spectroscopy (EDX, Oxford Instruments INCA), attached to a SEM (Zeiss EVO 50). The elemental composition was examined by energy dispersive X-ray spectroscopy (EDX, Oxford Instruments INCA), attached to a SEM (Zeiss EVO 50). The accuracy of measured content of metals such as Ti or Al by EDX is better than 1 at %. The content of Ar and O in the coatings was less than 1 at %. Wavelength-dispersive X-ray spectroscopy using an Oxford Instruments Inca analyzer under an acceleration voltage of 10 kV verified the consistency of the N content at different applied bias within the system specific sensitivity factors. The samples were subsequently annealed in vaccum at 950 and 1050 °C for 20 min (base pressure $<5\times10^{-4}$ Pa) with a heating and cooling rate of 20 °C/sec. For the diffraction experiment, a 100 µm slice was cut out from a sample in its as-deposited and annealed state, perpendicular to the sample surface. In a following step it was mechanically thinned down to a thickness of approximately 30 µm. The thickness uniformity has been verified by scanning electron microscopy.

The diffraction experiment was performed at the Nanofocus endstation of MiNaXS (P03) beamline of the PETRA III synchrotron radiation source at DESY, Hamburg (Germany) [20,21]. A schematic description of the experimental setup is given in Fig. 1. The experiment was performed in transmission mode using a monochromatic beam at a photon energy of 15.3 keV (λ = 0.0808 nm). A beam size in the sub-micron regime was achieved at the sample using a nanofocusing Kirkpatrick-Baez mirror system [22]. The beam was focused to a pencil shape with a height of 300 nm and a width of 1500 nm (determined at full width of half maximum of the beam). The sample was positioned into the beam using a hexapod with the coating oriented vertically, in order to benefit from the smaller horizontal dimension of the beam to obtain high spatial resolution along the coating depth profile. The vertical size was used to increase the scattering volume without compromising the spatial resolution. High resolution scans were performed using a linear XY piezo-positioner installed on the top of the hexapod (10 nm precision) translating the sample along its coating thickness in 100 nm steps. Diffraction images were recorded using a Photonics Science Imagestar 9000 high-resolution CCD camera with an input size of 188.2 × 188.2 mm² and a pixel size of 61.6 × 61.6 µm² (point-spread function 68.5 µm) at a sample-to-detector-distance of 193 mm with a typical exposure time of 10 seconds. The two dimensional (2D) diffraction data were subsequently processed using the Fit2D program package [23].

The phase evolution was obtained from integrated intensities of the diffraction patterns along the azimuthal angle δ in the range of 60 - 120 deg (Fig. 2). The center of this azimuthal area corresponds to the diffraction vector orientation parallel to the interface. In addition, the recorded 2D diffraction patterns from the position-resolved scanning

X-ray diffraction experiment were also used to calculate the local stress profiles across the coating thickness by dividing the full diffraction ring into cakes of 10 °, each being integrated separately to assess the azimuthal position dependence of the peaks. In order to evaluate the residual strain in the coating, three-dimensional dependencies of the lattice parameter (azimuthal angle, coating depth) were evaluated from the positions of the c-TiAlN 200 and c-Ti(Al)N 200 reflections corresponding to the coating in its as-deposited and annealed state, respectively. Strain was evaluated for each coating depth from the slope of d-$\sin^2\psi$ plots (where ψ is the angle between the sample normal and diffraction vector and d is the lattice spacing), which represents the distortion of the Debye-Scherrer ring from the circular shape [5,24,25]. Individual d-$\sin^2\psi$ plots included 36 measurement points corresponding to the same number of cake integrations along the Debye-Scherrer rings. The in-plane stress was calculated from the measured X-ray elastic strain according to X-ray diffraction Hooke´s law by using elastic stiffness constants for C_{11}, C_{12} and C_{44} of 458, 153 and 211 GPa [26], respectively and Hill grain interaction model. Since the Zener’s anisotropy ratio is about 1.4, the texture gradient across the coating was neglected for simplicity when calculating stresses from strains. Investigations by finite element calculation reported in [5] revealed only limited stress relaxation (less than 10%) during preparation of the sample slices for the diffraction experiments for the given slice geometry.

The relative intensity of the individual Debye-Scherrer rings was used to determine volume fractions of w-AlN precipitates in the sample after annealing at 1050 °C. These fractions were estimated from the intensities of the corresponding 10.0 diffraction peaks for the different measurement positions. As the intensity of all diffracting crystallites is spread along the Debye-Scherrer ring, the full ring intensity was summed up for every coating depth to determine the distribution of w-AlN formed across the coating thickness. In addition, density functional theory based calculations were performed using the Vienna Ab-initio Simulation Package (VASP) to obtain optimized crystal structure (atom positions and lattice parameters), bulk modulus and energy of formation of the TiAlN system as the function of the AlN mole fraction (for details see Ref. [27]). The isobaric mixing enthalpy of c-TiAlN with respect to pure c-TiN and c-AlN using an analytical expression from Ref. [28] has been calculated, being a measure of the thermodynamical driving force for the isostructural decomposition, and compared to the experimentally observed decomposition behavior.

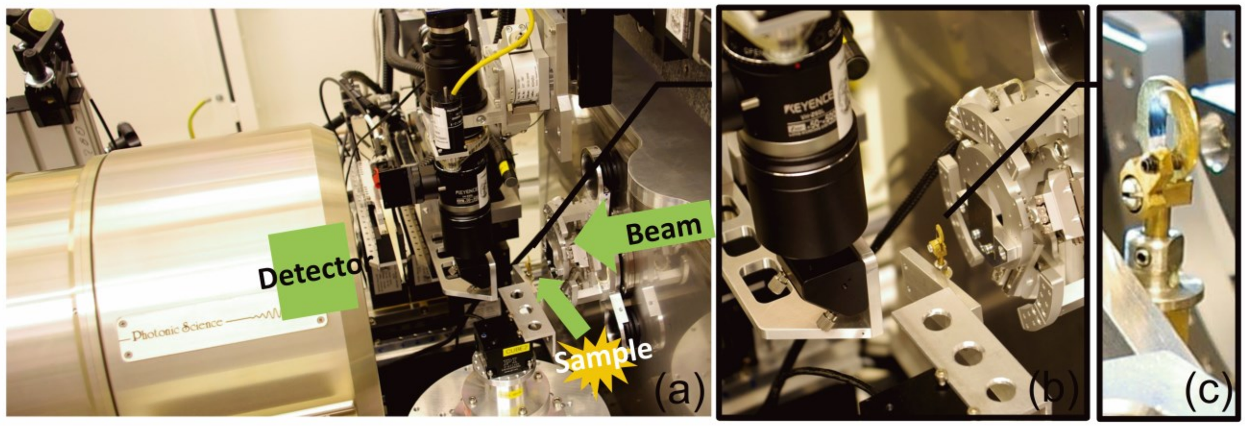

Fig. 1: *A photograph of the position-resolved cross-sectional X-ray diffraction setup (a) at the Nanofocus endstation of MiNaXS at P03 beamline (Petra III / DESY) with details of the sample positioning (b) and the sample holder with the sample (c).*

3. Results and Discussion

2D diffraction patterns revealed that the as-deposited TiAlN coating consists of face-centered cubic phase. The elemental composition along the coating cross-section determined by EDX was found to be constant and nearly stoichiometric with the Ti content marginally higher than the Al content (i.e., c-$Ti_{0.54}Al_{0.46}N$). Only a slight variation in the Al and N content within the coating was observed.

Cross-sectional SEM micrographs (Fig. 2) reveal alterations in morphology across the coating thickness associated with the variation of the energy of the incident ions during coating growth controlled by the applied negative bias voltage. The high flux of incident energetic particles during coating growth affects atomistic processes through enhanced surface diffusion of adatoms and also contributes to formation of structural defects [29]. The extent to which coating growth is affected depends on the energy distribution of the incident particles. Thus, the coating grown at -40 V bias is characterized by fine crystallites developed from many nuclei initially formed at the substrate-coating interface, which further develop with a needle-like shape (section I in Fig. 2). The competitive growth between coexisting grains in the next growth stages resulted in the development of columnar grains forming a typical V-shaped coating morphology (see section III in Fig. 2). Although the coating grew continuously with increasing grain size, a change of the coating morphology is obvious after reaching critical ion energy at -100 V bias voltage. The formation of a high number of structural defects gives rise to disruption of the continuous growth of individual grains and to the development of a fine-grained microstructure. This effect is much more pronounced in the uppermost fraction of the coating grown at -120 V, which is composed of small globular grains (see section V of Fig. 2).

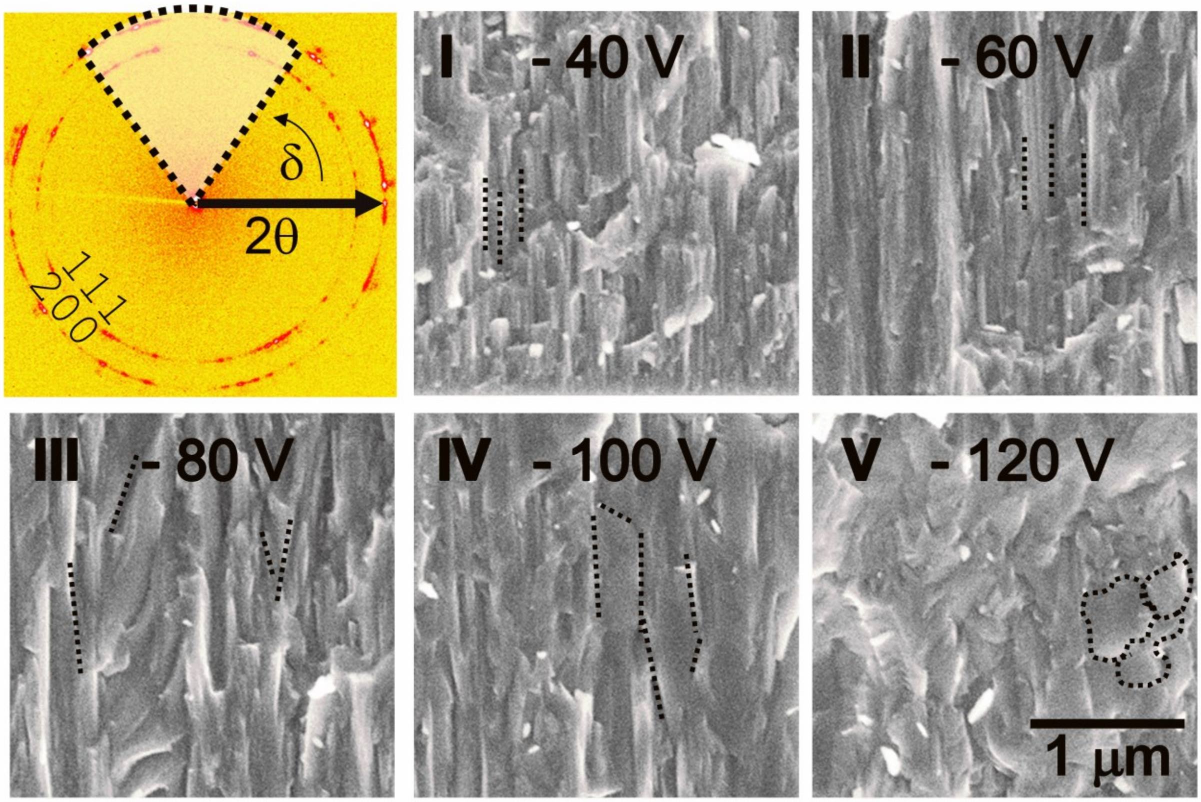

Fig. 2: *A representative Debye-Scherrer ring (a) recorded by position-resolved X-ray diffraction. 2θ represents ring radius whereas the shape of the ring is an indicator for locally present residual stress state. The section highlighted by dots indicates the azimuthal angle δ integration area used for the phase analysis (Fig. 3). For δ = 90 deg,*

the diffraction vector is oriented parallel to the interface. SEM cross-sectional micrographs of representative parts of the as-deposited coating depict in detail the morphological alterations of the coating fracture surface originating from the variation of the energy of incident particles during coating growth: (I) area near the interface grown at -40 V (with fine-grained to needle-like columnar microstructure), (II) - (IV) coating grown at -60 - -100 V (with equiaxed to V-shaped columnar microstructure) and (V) top section of the coating grown at -120 V (with fine granular (or globular) microstructure).

The phase and microstructure evolution of as-deposited and annealed c-TiAlN coatings across their depth were determined by analyzing the positions and shapes of Bragg's reflections (Fig. 3). In the as-deposited state, the coating is entirely single-phase cubic (Fig. 3a). The shift of the diffraction peaks to lower 2θ angle in 3 μm steps reflects the increase of the interplanar spacing of TiAlN crystallographic planes. This expansion is related to the generation of an increasingly higher amount of point defects with increasing irradiation-energy resulting in the lattice parameter expansion. This is also reflected by the diffraction peaks broadening, associated with a decrease of the grain size and/or an increase of the strain of the 2nd and 3rd order. The coating remained single-phase cubic also after annealing at 950 °C (Fig. 3b). Although the energetic input into the coating by heating is not sufficient to induce decomposition of the metastable c-TiAlN solid solution, it is sufficiently high to activate the recovery of the disordered structure [18]. The recovery of growth defects is obvious in the change of the position and shape of the diffraction peaks across the coating depth. While the peaks shift to higher 2θ angles, their widths change only slightly, which indicates that the grain size remains unchanged and/or the strain of 2nd and 3rd order does not change at this temperature. The peak shift can be interpreted by the relaxation of unstressed lattice parameter and/or changes in residual stress state [18]. After annealing at 1050°C, decomposition of c-TiAlN into TiN-rich and AlN-rich cubic domains, which coexist with segregated w-AlN precipitates, was observed [8]. This process is reflected by a split of the diffraction peaks corresponding to c-TiAlN into two newly appearing reflections corresponding to c-Ti(Al)N and c-Al(Ti)N and by the appearance of 10.0, 00.2 and 10.1 diffraction peaks of w-AlN (Fig. 3c).

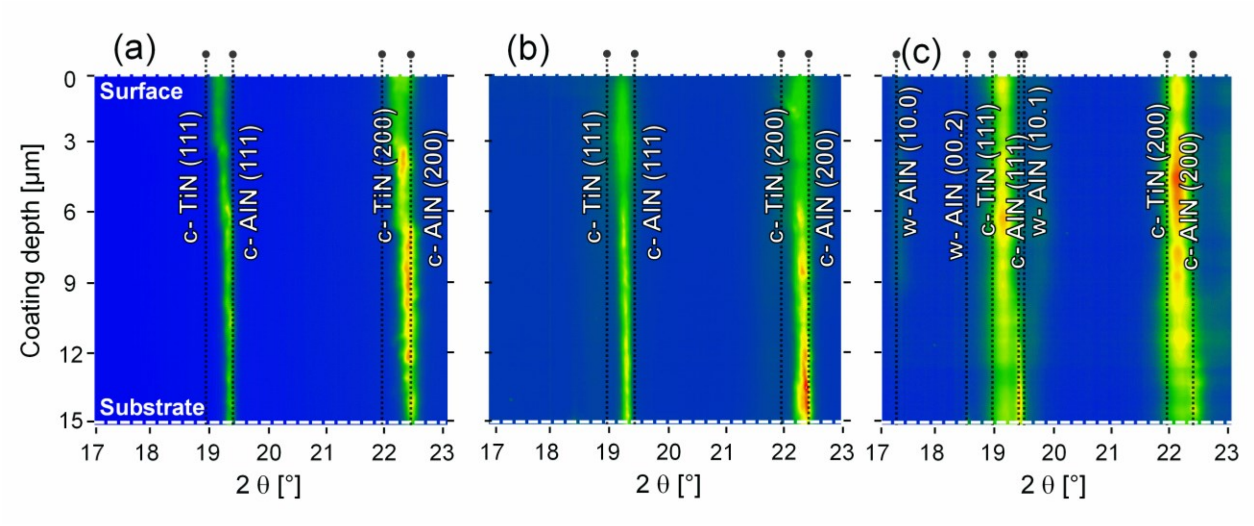

Fig. 3: Phase evolution as a function of the TiAlN coating depth in as-deposited state (a) and after annealing at 950 °C (b) and 1050 °C (c).

Besides the phase and microstructure analysis, the possibility to determine position-resolved stress profiles is the main benefit of the method. A full fingerprint of the residual stress state in the coating as a function of the coating depth is obtained from the analysis of the elliptical distortions of the recorded Debye-Scherrer rings [5]. The stress distributions across the as-deposited and at 950°C annealed coatings were determined from the positions of the c-TiAlN 200 reflections. The stresses (in the cubic phase) in the coating annealed at 1050 °C were evaluated from the c-Ti(Al)N 200 reflections. The stress distributions across the as-deposited as well as the annealed samples are presented in Fig. 4. The stress of the coating in the as-deposited state changes from tensile to compressive with decreasing depth (corresponding to the increasing substrate bias) (Fig. 4a). Tensile stress near the substrate originates from the dominant contribution of the thermal tensile stress, caused by the mismatch of the thermal expansion coefficients α of the substrate and the coating (since $\alpha_{\mathrm{TiAlN}} = 7.5 \times 10^{-6}\ \mathrm{K}^{-1}$ [30] is higher than $\alpha_{\mathrm{WC\text{-}Co}} = 5.0 \times 10^{-6}\ \mathrm{K}^{-1}$ [31]), over the negligible compressive intrinsic growth stress associated with ion-assisted coating growth. With increasing ion energy the number of structural defects increases, which results in generation of compressive stress [32]. As the compressive intrinsic stress component exceeds the tensile thermal stress component (at the depth of about 9 μm), the overall stress becomes compressive. This effect is more pronounced for more intense irradiation conditions. The change in the deposition conditions at individual stages, as the bias voltage and thus the ion energy were increased, is reflected by an approximately step-wise nature of the stress profile. The oscillations of the stress dependence within the coating sections grown under the same conditions (Fig. 4a) can be related to the development of the coating microstructure through competitive growth. In fact, grain coarsening is accompanied by a subsequent reduction of the volume fraction of grain boundaries, which are more sensitive to displacement of atoms during coating growth. Thus, a decrease of the number of grain boundaries results in a decrease of the compressive stress in these areas [33]. The variation of the grain size is thus reflected by a variation of the residual stress. An additional contribution to the local variation of the stress state may be the local change of the texture [34], which was, however, not easily to be identified from this experiment and therefore not discussed here.

Annealing of the coating at 950 °C for 20 min results in a further relaxation of the growth stresses, which is indicated by a shift of the diffraction peaks to higher 2θ angles (Fig. 3b) and by a reduction of the stress state (Fig. 4b). The stress in the low bias area is almost fully relaxed after annealing. The WC-Co substrate is assumed to not deform plastically during the annealing treatment; thus, the relaxation of tensile stress is probably promoted by cobalt diffusion at the substrate-coating interface. The sections of the coatings grown under more intense ion irradiation are still under compressive stress, which is attributed to defects of higher thermal stability generated at higher bias voltage [35,36]. They can be assumed to inhibit defect recovery to a different extent due to microstructure-dependent diffusion processes, noticeable by a pronounced local variation of the stress state in the -120 V coating fraction. Full stress relaxation would thus be accomplished after longer annealing time, when the defect recovery is completed.

The stress profile in the coating after annealing at 1050 °C for 20 min, showing a change from a high tensile to a high compressive stress state across its thickness (Fig. 4c), is attributed to the phase decomposition of the metastable c-TiAlN solid solution. While coating sections grown under moderate ion irradiation are under tensile stress, compressive stress developed in the coating sections exposed during growth to a high-energy sputter flux (Fig. 3). The development of tensile stress can be attributed to the volume reduction caused by the formation of Al-rich domains within the entire c-TiAlN matrix at an early stage of spinodal decomposition [12]. As the coating adheres on the rigid WC-Co substrate material, the c-Ti(Al)N phase appears to be put under tension after annealing to 1050 °C. On the contrary, the compressive stress development in the uppermost fraction of the coating is due to the formation of first w-AlN precipitates (Fig. 3c), which typically develop in the further stages of the spinodal decomposition from the metastable c-Al(Ti)N. As they exhibit higher specific volume compared to the cubic structure, the area surrounding the w-AlN precipitates is compressed. The highest compressive stress is found in the -80 V section, being the fraction with moderate irradiation conditions. This clearly indicates a stress-dependent kinetics of phase decomposition of metastable supersaturated c-TiAlN.

The volume fraction of w-AlN precipitates formed in the coating after annealing at 1050 °C influence decisively the residual stress state of the deposit. It was evaluated by a summation of the relative peak intensity from the full ring integration of the predominately [10.0] oriented w-AlN phase and is shown in Fig. 5a. The precipitates are evidently preferentially formed in the -80 V bias section, i.e. a coating section grown under moderate ion irradiation conditions. This is in a good agreement with the residual stress profile developed after annealing at 1050 °C (Fig. 4c), where the highest compressive stress followed by its decrease with increasing bias voltage well corresponds to the formation of the w-AlN precipitates.

To explain the variation of the thermal stability across the thickness of the gradient TiAlN coating, a mechanism based on the interplay of two effects – first, one which boosts and second, one which retards the decomposition of c-TiAlN – is proposed. On the one hand, the isostructural formation of c-Al(Ti)N domains, which require less volume than c-Ti(Al)N domains [11], is promoted by compressive stress [37]. This in turn leads to an increased amount of c-Al(Ti)N domains, which subsequently transform into w-AlN precipitates. On the other hand, this phase transformation is retarded as it is accompanied by a ~24% specific volume increase [38]. In highly compressively stressed areas, the strain energy corresponding to the cubic-to-wurtzite transformation volume increase is high, subsequently constraining the phase decomposition. This fact allows to control the cubic-to-wurtzite phase transformation by the adjustment of thermally or irradiation-induced compressive stress.

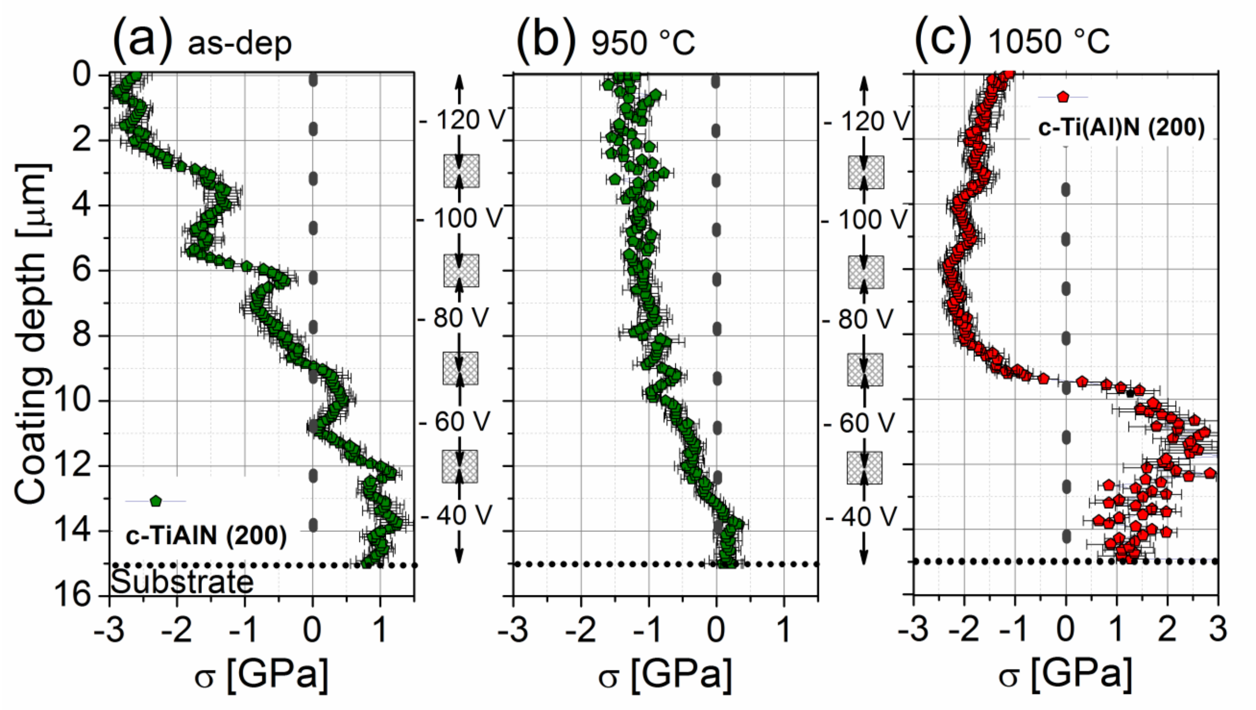

Fig. 4: Residual stress distribution across the thickness of the as-deposited (a) and at 950 °C (b) and 1050 °C (c) annealed samples. The shaded areas mark the near interface regions between the individual bias voltage settings.

In order to gain a quantitative insight into the proposed scenario, density functional theory calculations are employed. Fig. 5b shows the isobaric mixing enthalpy of c-TiAlN with respect to c-AlN and c-TiN, which is a measure of the thermodynamical driving force for isostructural decomposition, versus the pressure (i.e. hydrostatic compression) in the cubic allotrope. This represents a simplified situation to the real bi-axial compressive stresses introduced in the coating by high-energy ions. The mixing enthalpy values for the decomposition of c-TiAlN into c-AlN and c-TiN increases with pressure, which indicates that isostructural decomposition is promoted by higher compressive stress at a given temperature and annealing time. Fig. 5b also depicts the pressure-dependent differences of the energy for the c- into w-AlN phase transformation. In principle, the higher this energy difference is, the more is the formation of the wurtzite phase favored. A decrease with the increasing pressure represents a reduced thermodynamical driving force for the cubic-to-wurtzite transformation. Thus, it can be concluded that a higher compressive stress, represented by the pressure in Fig. 5b, effectively retards precipitation of w-AlN. These two effects compete so that the volume fraction of w-AlN differs in the coating depending on its stress state. The local changes of the amount of w-AlN precipitates in the coating follows the arguments above - a low volume fraction of w-AlN precipitates is present in tensile or low compressively stressed parts of the coating while a higher fraction is formed in areas with moderate compressive stress (corresponding to the sections of the coating grown at -80 to -120 V bias voltage). As a certain threshold of the compressive stress is exceeded, the retarding effect becomes dominant resulting in an again reduced fraction of w-AlN precipitates (see Fig. 5a).

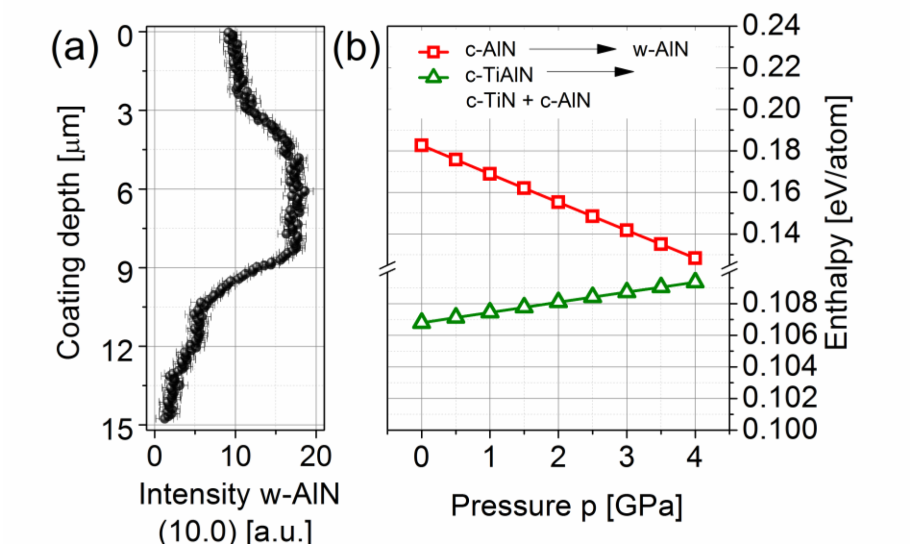

Fig. 5: Relative intensities of the w-AlN 10.0 reflections as a function of the coating depth indicate varying volume fractions of w-AlN precipitates in different coating regions. The most intensive w-AlN formation was observed in the area prepared using negative bias voltage of 80 V. (b) Ab inito calculations of the isobaric driving force of c-TiAlN → c-

TiN + c-AlN decomposition with increasing compression and c-AlN → w-AlN energy difference at constant volume.

Besides the stress state, also the microstructure plays a crucial role in the thermal stability of TiAlN coatings, which significantly changes according to the growth conditions adjusted by the applied bias voltage. Intense irradiation conditions result in structural refinement and generation of high defect density (see Fig. 2, sections IV-V), which is reflected by the distinct peak broadening (Fig. 3a). This is commonly associated with formation of strain of higher order, lattice defects and/or reduction of the grain size. Thus, in the -80 V section, which exhibits moderate stress but well developed grains compared to other coating sections (see Fig. 2, section III), phase transformation is favored (see Fig. 5a).

4. Conclusion

The depth-dependent evolution of microstructure, residual stresses and their relation to the phase stability of a stepwise graded TiAlN coating has been investigated by a combinatorial X-ray sub-micron diffraction method. The decomposition behavior of the coating during annealing is given by the variation of the ion energy, predetermining its initial microstructure and residual stress state, which control the local stress relaxation as well as the formation of precipitates. Increasing ion energy leads to an increasing compressive intrinsic stress component formed in the coating resulting in a change of the residual stress state from tensile into compressive with increasing ion energy. Annealing of the coating results in preferred recovery of defects of low thermal stability, formed at lower ion energy. The volume fraction of w-AlN precipitates, formed during phase transformation differs in the individual coating sections evidently depending on the initial microstructure and stress state. This is more favored the higher the ion energy is, depicting a maximum in regions characterized by low stress and well-developed grains; at even higher ion energy, depicting higher compressive stress, it is retarded demonstrating non-linear behavior. In this study it has been shown in a depth-dependent way how local microstructure, adjusted by ion irradiation conditions and residual stress state of the coating determine the thermal stability of the coating. The results demonstrate the ability of cross-sectional scanning X-ray diffraction as a powerful method to determine local microstructure and properties, providing the basis for the establishment of structure-property relationships in heterogeneous materials and for their further improvement.

Acknowledgement

Gabriele Moser (Erich Schmid Institute of Materials Science, Austrian Academy of Sciences) is acknowledged and thanked for sample preparation. Financial support by the Austrian Federal Government (in particular from Bundesministerium für Verkehr, Innovation und Technologie and Bundesministerium für Wirtschaft, Familie und Jugend) represented by Österreichische Forschungsförderungsgesellschaft mbH and the Styrian and the Tyrolean Provincial Government, represented by Steirische Wirtschaftsförderungsgesellschaft mbH and Standortagentur Tirol, within the framework of the COMET Funding Programme is gratefully acknowledged. The nano-focus end-station was equipped through financial support by the German Federal Ministry of Education and Research (BMBF projects 05KS7FK3 and 05K10FK3) which is also greatly acknowledged. We thank the P03 team for provision of the beam to the nanofocus end station. D.H. acknowledges financial support from the Austrian Science Fund (FWF) through the START Program (Y371).

References

[1] A. Cavaleiro, J.Th.M. DeHosson (Eds), Nanostructured Coatings, Springer, New York, 2006.

[2] P.H. Mayrhofer, C. Mitterer, H. Clemens, Adv. Eng. Mater. 7 (2005) 1071.

[3] J. Keckes, R. Daniel, C. Mitterer, I. Matko, B. Sartory, A. Koepf, R. Weißenbacher, R. Pitonak, Thin Solid Films 545 (2013) 29.

[4] J. Keckes, M. Bartosik, R. Daniel, C. Mitterer, G. Maier, W. Ecker, J. Vila-Comamala, C. David, S. Schoeder, M. Burghammer, Scripta Mater. 67 (2012) 748.

[5] M. Stefenelli, J. Todt, A. Riedl, W. Ecker, T. Müller, R. Daniel, M. Burghammer, J. Keckes, J. Appl. Crystallogr. 46 (2013) 1378.

[6] M. Bartosik, R. Daniel, C. Mitterer, I. Matko, M. Burghammer, P.H. Mayrhofer, J. Keckes, Thin Solid Films 542 (2013) 1.

[7] W.D. Münz, J. Vac. Sci. Technol. A4 (1986) 2717.

[8] P.H. Mayrhofer, A. Hörling, L. Karlsson, J. Sjölen, T. Larsson, C. Mitterer, L. Hultman, Appl. Phys. Lett. 83 (2003) 2049.

[9] K. Kutschej, P.H. Mayrhofer, M. Kathrein, P. Polcik, R. Tessadri, C. Mitterer, Surf. Coat. Technol. 200 (2005) 2358.

[10] A. Hörling, L. Hultman, M. Odén, J. Sjölen, L. Karlsson, Surf. Coat. Technol. 191 (2005) 384.

[11] N. Schalk, C. Mitterer, J. Keckes, M. Penoy, C. Michotte, Surf. Coat. Technol. 209 (2012) 190.

[12] J.M. Andersson, J. Vetter, J. Müller, J. Sjölen, Surf. Coat. Technol. 240 (2014) 211.

[13] R. Rachbauer, E. Stergar, S. Massl, M. Moser, P.H. Mayrhofer, Scripta Mater. 61 (2009) 725.

[14] R. Rachbauer, S. Massl, E. Stergar, D. Holec, D. Kiener, J. Keckes, J. Patscheider, M. Stiefel, H. Leitner, P.H. Mayrhofer, J. Appl. Phys. 110 (2011) 023515.

[15] Ch. Wüstefeld, D. Rafaja, M. Dopita, M. Motylenko, C. Baehtz, C. Michotte, M. Kathrein, Surf. Coat. Technol. 206 (2011) 1727.

[16] P.H. Mayrhofer, D. Music, J.M. Schneider, Appl. Phys. Lett. 88 (2006) 071922.

[17] P.H. Mayrhofer, F.D. Fischer, H.J. Böhm, C. Mitterer, J.M. Schneider, Acta Mater. 55 (2007) 1441.

[18] M. Bartosik, R. Daniel, Z. Zhang, M. Deluca, W. Ecker, M. Stefenelli, M. Klaus, C.Genzel, C. Mitterer, J. Keckes, Surf. Coat. Technol. 206 (2012) 4502.

[19] L. Rogström, J. Ullbrand, J. Almer, L. Hultman, B. Jansson, M. Odén, Thin Solid Films 520 (2012) 5542.

[20] C. Krywka, H. Neubauer, M. Priebe, T. Salditt, J. Keckes, A. Buffet, S. Roth, R. Doehrmann, M. Mueller, J. Appl. Crystallogr. 45 (2012) 85.

[21] A. Buffet, A. Rothkirch, R. Dohrmann, V. Korstgens, M. Kashem, J. Perlich, G. Herzog, M. Schwartzkopf, R. Gehrke, P. Muller-Buschbaum, S. Roth, J. Synchrotron Radiat. 19 (2012) 647.

[22] C. Krywka, J. Keckes, S. Storm, A. Buffet, S. Roth, T. Döhrmann, M. Müller, J. Phys. Conf. Ser. 425 (2013) 072021.

[23] A.P. Hammersley, S.O. Svensson, M. Hanfland, A.N. Fitch, D. Häusermann, High Pressure Res. 14 (2006) 235.

[24] B.B. He, Two-dimensional X-Ray Diffraction, Wiley, New Jersey, 2009.

[25] D. Waterman, G. Evans, J. Appl. Cryst. 43 (2010) 1356.

[26] F. Tasnádi, A.I. Abrikosov, L. Rogström, J. Almer, M. Johansson, M. Odén, Appl. Phys. Lett. 97 (2010) 231902.

[27] D. Holec, R. Rachbauer, L. Chen, L. Wang, D. Luef, P.H. Mayrhofer, Surf. Coat. Technol. 206 (2011) 1698.

[28] D. Holec, F. Rovere, P.H. Mayrhofer, P.B. Barna, Scripta Mater. 62 (2010) 349.

[29] I. Petrov, L. Hultman, U. Helmersson, J.E. Sundgren, Thin Solid Films 169 (1989) 299.

[30] L.E. Toth, Transition Metal Carbides and Nitrides, Academic Press, New York, 1971.

[31] P. Hindert, J. Res. Nat. Bur. Stand. 18 (1937) 47.

[32] C.A. Davis, Thin Solid Films 226 (1993) 30.

[33] R. Daniel, K.J. Martinschitz, J. Keckes, C. Mitterer, Acta Mater. 58 (2010) 2621.

[34] R. Daniel, J. Keckes, I. Matko, M. Burghammer, C. Mitterer, Acta Mater. 61 (2013) 6255-6266.

[35] P.H. Mayrhofer, C. Mitterer, Surf. Coat. Technol. 133-134 (2000) 131.

[36] L. Karlsson, A. Hörling, M.P. Johansson, L. Hultman, G. Ramanath, Acta Mater. 50 (2002) 5103.

[37] B. Alling, M. Odén, L. Hultman, A.I. Abrikosov, Appl. Phys. Lett. 95 (2009) 181906.

[38] N.E. Christensen, I. Gorczyca, Phys. Rev. B 47 (1993) 4307.

Publication III

Resolving Depth Evolution of Microstructure and Hardness in Sputtered CrN Film

A. Zeilinger, R. Daniel, T. Schöberl, M. Stefenelli, B. Sartory, J. Keckes, C. Mitterer

Submitted for publication.

Resolving Depth Evolution of Microstructure and Hardness in Sputtered CrN Film

A. Zeilinger[a], R. Daniel[b], T. Schöberl[c], M. Stefenelli[a], B. Sartory[a], J. Keckes[c], C. Mitterer[b]

[a] *Materials Center Leoben Forschung GmbH, Roseggerstraße 12, 8700 Leoben, Austria*

[b] *Department of Physical Metallurgy and Materials Testing, Montanuniversität Leoben, Franz-Josef-Straße 18, 8700 Leoben, Austria*

[c] *Erich Schmid Institute of Materials Science, Austrian Academy of Sciences and Department of Materials Physics, Montanuniversität Leoben, 8700 Leoben, Austria*

Abstract

Hardness and elastic modulus of a sputtered nanocrystalline CrN thin film, prepared under varying ion bombardment conditions, was studied by nanoindentation using a depth-profiling technique and related to cross-sectional X-ray nanodiffraction data on the local microstructure. Changes in texture are shown to have almost no effect on the elastic modulus due to the isotropic response of the polycrystals. However, the locally varying growth conditions, which affect the crystal size and the number of defects in the film, determine the hardness values across the film thickness. Regions with highly distorted small crystals result in higher hardness in comparison to those with well-developed coarsened grains. This study confirms the notion of the existence of growth-related hardness gradients in single-phase nanocrystalline thin films.

Keywords:

Hardness; Microstructure; Gradient; X-ray nanodiffraction; Film growth; CrN;

1. Introduction

Nanocrystalline thin films grown by plasma-assisted vapor deposition have attracted huge interest due to their outstanding properties, making them suitable for various applications ranging from wear protection to semiconductor devices [1,2,3]. Their uniqueness can be attributed to their growth under non-equilibrium deposition conditions, which, however, typically results in an inhomogeneous microstructure in terms of phases and morphology as well as crystallite size, texture and structural defects.

To determine the dominant atomistic processes affecting the microstructural evolution of thin films, extensive pioneering work has been done in the last decades to generate a basic understanding of the structure formation at the micro-scale. Investigations regarding process-related film microstructure have been comprehensively summarized in structure zone models (SZM), which discuss the influence of growth parameters, e.g. deposition temperature, gas pressure, bias potential, on structural film evolution in detail [4,5,6,7].

A prerequisite for the understanding of microstructure evolution has been the development of sophisticated local analysis techniques such as high-resolution transmission electron microscopy. The technique allows nano-scale characterization of thin films as shown in [8]. With the implementation of cross-sectional X-ray nanodiffraction, new insights into the microstructure of thin nanocrystalline films have been gained, revealing them to be extremely complex regarding crystallographic texture and crystallite size [9]. The technique also allows to determine position-resolved data on the depth gradients [10,11] of residual stresses, which are a consequence of changes in the microstructure evolution during film growth [12].

The microstructure of thin films has been shown to crucially determine their mechanical properties [13]. As thin films are often subjected to severe loading conditions, the establishment of correlations between microstructure and mechanical properties, especially the hardness, is of vital importance. Conventional hardness measurements using nanoindentation devices are surface sensitive; therefore, approaches to determine hardness depth-profiles have been developed, in particular for multilayer arrangements [14,15]. Knowledge about the local variation of microstructure and hardness in a film grown by plasma-assisted vapor deposition can be essential for their further improvement; however, an approach to illuminate this relationship with sub-micron resolution is not available up to now, due to the lack of characterization methods with the necessary resolution.

Within this study, nanoindentation has been performed using a depth-profiling technique on thin nanocrystalline CrN films, exhibiting varying ion bombardment conditions during growth. The obtained hardness and elastic modulus variations are related to position-resolved cross-sectional X-ray nanodiffraction data, providing local information on crystallographic texture and grain size. This study contributes to the basic understanding of hardness evolution of polycrystalline CrN films with the locally varying growth conditions across the film thickness.

2. Experimental Details

A nanocrystalline CrN film was grown on chemically pre-cleaned single crystal Si (100) substrates, located at a distance of 20 cm from the target, by reactive magnetron sputtering in an Oerlikon Balzers INNOVA deposition system using a powder metallurgically prepared Cr target (99.99% purity, Plansee Composite Materials). The CrN film was synthesized at a total pressure of 1 Pa in an Ar + N2 gas mixture with a nitrogen partial pressure of 0.25 Pa, a target power of 6 kW and a substrate temperature of 350 °C. A microstructural gradient in the film growth direction was achieved by adjusting the negative bias voltage (also affecting the energy of the incident ions) to -40, -120 and -40 V in 5 µm steps. The total thickness of the film was set to 15 µm.

The microstructure of the film cross-section was investigated using a Zeiss LEO 1525 scanning electron microscope (SEM). In order to reveal the local mechanical properties of the inhomogeneous film across its thickness, a wedge-shaped depth profile was fabricated by focused ion beam (FIB) milling. The profile was prepared on a film/substrate fracture cross-section using an Orsay Physics Cobra Z-05 FIB apparatus, attached to a Zeiss Auriga 60 Crossbeam FEG-SEM. Before FIB milling, a Pt layer was deposited at the surface of the cross-section (see Fig. 1a) to protect the film from unintended material removal. Then, film material was locally removed in the shape of a rectangular slice in a distance of 50 µm from the fracture cross-section surface, using coarse milling conditions (voltage 30 kV, ion beam current 20 nA), to avoid material deposit at the film surface by the subsequent milling steps. Then, the focused ion beam was adjusted parallel to the film surface and a depth profile (length-depth ratio 9:1) was fabricated using fine milling conditions (30 kV, 4 nA), followed by a polishing procedure of the surface at even finer (30 kV, 600 pA) milling conditions (Fig. 1b). After the FIB procedure, the sample was fixed to an inclined steel plate to provide horizontal alignment [16] between the indenter and the surface (see inset in Fig. 1). The surface of the wedge to be indented was examined by energy-dispersive X-ray spectroscopy (EDX, Oxford Instruments INCA), attached to a SEM (Zeiss EVO 50).

The mechanical properties of the CrN film at different positions on the wedge (corresponding to different depths) were investigated by nanoindentation using a Hysitron Triboscope attached to an atomic force microscope (AFM, Veeco Instruments Dimension 3100). Measurements have been performed using a cube corner tip; its area function was determined by a series of indentations on fused silica. In rows, perpendicularly aligned to the wedge profile with mutual distances of 6 µm, at least 7 load-displacement curves for each row with a load of 10 mN were recorded, resulting in a maximum indentation depth of about 300 nm. The number of measurements was limited by the given space on the wedge surface, since interference of adjacent indents had to be avoided. Indentation hardness (H) and reduced elastic modulus (Er) were determined applying the Oliver and Pharr method [17].

A detailed microstructural analysis of the film was performed at the nanofocus extension of the ID 13 beamline [18] at ESRF in Grenoble, France. A detailed description of the experimental setup is given in [9]. The experiment was performed in transmission mode using a monochromatic beam at a photon energy of 13 keV being focused to 100 nm in diameter by Kirkpatrick-Baez mirrors. The sample was positioned with the film/substrate interface oriented parallel to the beam (sample thickness in beam direction 100 μm) and diffraction images were recorded with a sample-to-detector distance of about 10.2 cm using a CCD area detector with a resolution of 2048 × 2048 pixels. In order to scan the film cross-section, the sample was translated in the beam along its film thickness in 200 nm steps with a typical exposure time of 0.5 s. The two-dimensional (2-D) diffraction data was processed using the software package Fit2D [19].

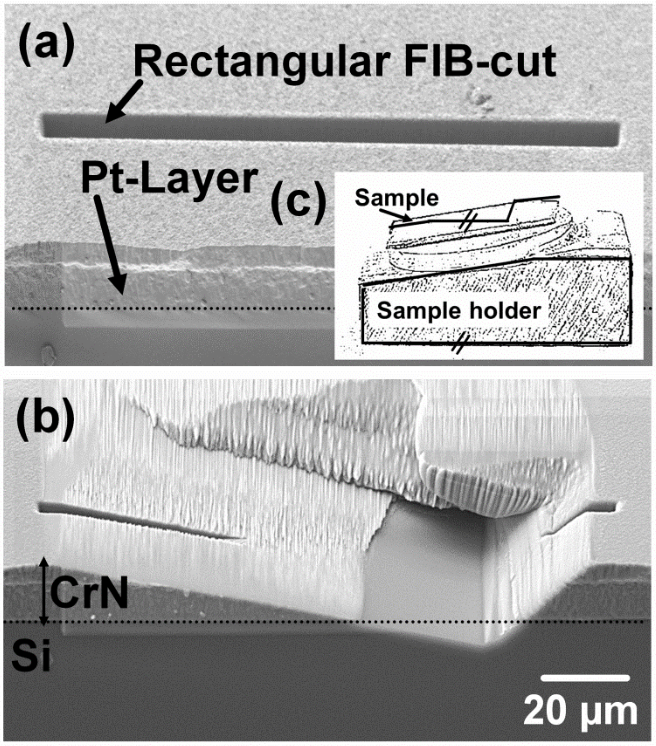

Fig. 1: *Fabrication of the film depth-profile with the FIB-technique: (a) preparation of a rectangular lift-out to avoid re-deposition and deposition of a Pt protection layer, (b) subsequent FIB milling of a wedge profile for nanoindentation, where no detectable Ga contamination at the surface was found, and (c) fixation of the sample on a tilted sample holder providing horizontal alignment of the film surface.*

3. Results

SEM revealed the film to exhibit a smooth and dense surface and a total film thickness of 15 µm. The average arithmetical surface roughness Sa on the wedge studied using AFM was less than 5 nm. The film exhibited a nearly stoichiometric composition (N/Cr = 1 - 1.09) and the crystallographic structure was determined to be single-phase face-centered cubic. Contamination by the Ga beam or Pt atoms from the protection layer was determined by an EDX line scan along the surface of the depth-profile and was found to lie in the range of the system-specific sensitivity factors.

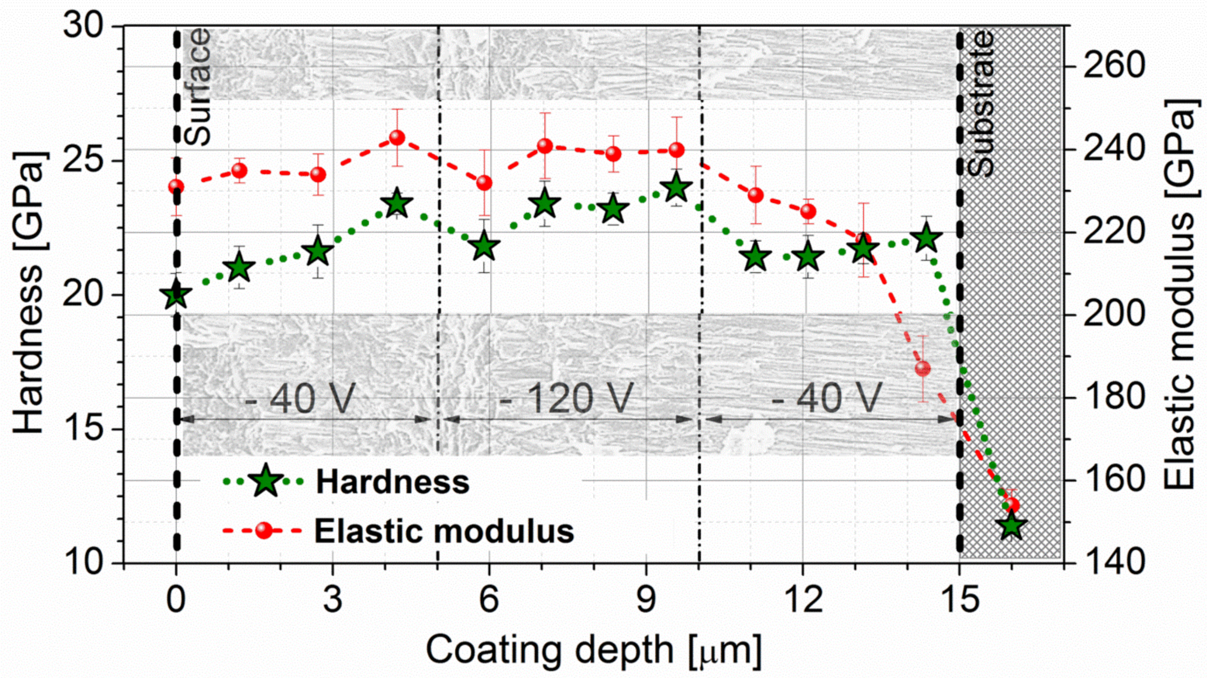

Fig. 2: *Dependence of hardness and reduced elastic modulus on film depth for a CrN film composed of three 5 µm thick sections grown at –40, –120 and –40 V bias.*

Fig. 2 displays the evolution of H and Er as a function of the increasing film thickness (or, which is equivalent, decreasing film depth). There, nanoindentation measurements were done on different positions on the wedge, corresponding to various film depths. In Fig. 2, the dark shaded area illustrates the substrate, and the H and Er evolution with increasing film thickness is plotted from right to left. Two clearly visible abrupt changes in mechanical properties can be identified, dividing the film into three sections, each about 5 µm in thickness. The values for H and Er within the individual sections also vary locally. H and Er of the substrate were determined to be 11 and 150 GPa, respectively. These values are together with the ones of the CrN film in good agreement with literature [20,21]. The Er/H ratio for the film is with a value of 10.5 almost constant down to a film thickness of about 5 µm. With further decrease of film thickness, Er is decreasing remarkably, indicating an increasing influence of the less stiff Si substrate during the indentation measurement. H is found to be ~22 GPa near to the substrate interface and is decreasing slightly with increasing film thickness. At a film thickness of about 5 µm, a sudden increase in H up to 24 GPa is observed, which is followed by an oscillating behavior of H up to a film thickness of 10 µm (H = 22 GPa). In the top region of the film, H is again high (H = 23.4 GPa) but decreasing rapidly with further increasing film thickness, reaching a minimum value of 20.5 GPa close to the film surface (i.e. at a film thickness close to 15 µm). The development of Er follows the behavior of the H, reaching maximum and minimum values of 240 and 180 GPa, respectively, where the latter value approaches the modulus of the Si substrate.

4. Discussion

The SEM micrograph of the fracture cross-section in Fig 3 provides first insight into the film microstructure. Three sublayers can be identified due to local differences in fracture behavior. In the following, these layers are denoted as bottom (-40 V bias), middle (-120 V bias) and upper (-40 V bias) section. Needle-like grains oriented perpendicular to the substrate surface are present in the bottom section of the film grown at -40 V applied bias. Increasing the ion bombardment to -120 V affects the microstructure of the film in the middle section, evidently featuring a more interrupted fracture cross-section [12]. The further reduction of the ion bombardment conditions to -40 V again changes the film morphology and needle-like grains are formed in the upper section of the film.

To gain insight into the microstructural evolution of the CrN film in the individual sections, the crystallographic texture has been characterized by extraction of pole figures from the cross-sectional X-ray nanodiffraction data (Fig. 3). 2-D azimuthal distributions of the intensities along the Debye-Scherrer rings have been evaluated using Wenk´s method [22] and orientation distribution functions have been reconstructed for individual measurement positions [23], enabling to distinguish different regions within the bottom, middle and upper film sections. The pole figures in Fig. 3 reveal that, close to the substrate interface (region I) the film grows fiber textured with (001) planes oriented parallel to the substrate surface, which corresponds to the thermodynamically favored crystallographic orientation of CrN with the lowest surface energy [24]. At 3 µm thickness, i.e. still in the bottom section, the (100) texture smoothly transforms into the (110) fiber texture (Fig. 3, region II), as the film develops by competitive growth predominately controlled by kinetic restrictions. In the middle section (i.e. at -120 V bias), one can observe a mixed (111) and (100) fiber texture (Fig. 3, regions III-V), which again transforms smoothly into the (110) texture in the top section (i.e. at -40 V bias) of the film (Fig. 3, regions VI-VII).

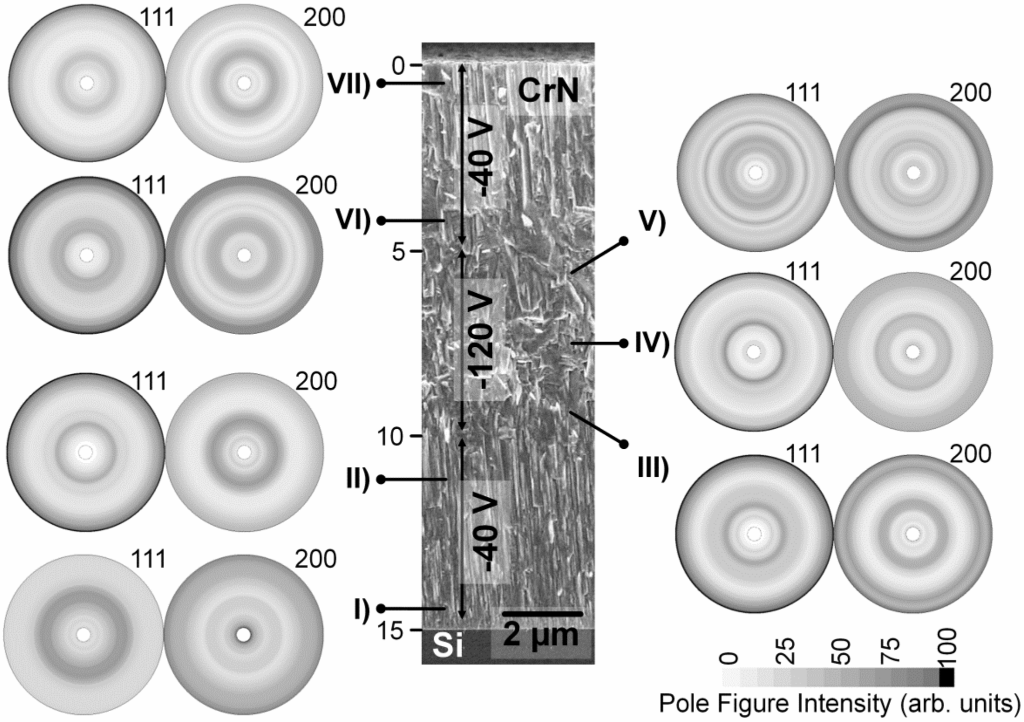

Fig. 3: SEM cross-section with CrN 111 and 200 pole figures indicating differences in film texture over thickness.

Considering CrN single crystal elastic constants c11=542, c12=27 and c44=88 GPa [25], the Zener's anisotropy ratio A = 2c44/(c11-c12) is 0.342. This documents that CrN is stiffest along the <100> and softest along the <111> crystallographic directions. Since the film exhibits, as shown above, a strong variation of texture, one could expect that elastic anisotropy will influence also the elastic modulus significantly. Close to the substrate interface (region I), the indentation occurs along the <100> direction of the crystallites, which is the stiffest one. The measured values of the modulus are nevertheless relatively small, which evidences already the influence of the soft Si substrate. In the middle and the upper section of the thin film, Er is almost constant, which can be interpreted by the isotropic response of the polycrystal. It should be noted that – in spite of the present texture - by using nanoindentation it is not possible to distinguish between the orientation-dependent elastic properties of anisotropic materials [26,27].

Consequently, the development of the hardness is related to the unique thin film microstructure evolution across the film thickness. At 0, 5 and 10 μm film thickness (Fig. 2, curve highlighted by stars), the hardness exhibits local maxima and then decreases within individual sublayers. This effect correlates well with the morphology of the crystallites and the full width at half maximum (FWHM) development of the diffraction peaks illustrated in Fig. 4a. There, FWHM represents the average size of the crystalline domains in the direction of the diffraction vector. The data is plotted in dependence of the tilting angle ψ (corresponding to in- and out-of-plane diffracting planes) and the film thickness, which allows a 2-D reconstruction of the grains [9].

At the substrate interface film nucleation takes place; consequently, the crystallite size is relatively small as documented by the large FWHM values, resulting in a high hardness [28]. Most probably, an even higher value can be assumed in this region (I) of the film as the hardness might be affected by the softer Si substrate, as the usually accepted 10 % indentation depth rule is exceeded [16]. As the film grows, a columnar microstructure with larger crystallites develops (see Fig. 4b, -40 V) and consequently hardness decreases, according to the Hall-Petch effect [29,30]. This is indicated also by the small FWHM values for near out-of-plane and large values for in-plane orientation, caused by the aspect ratio of the needle-like CrN nanocrystals. When the ion bombardment intensity is increased by raising the applied bias potential to -120 V, a high number of defects is generated [31], which results in a distorted film microstructure. In the middle section of the thin film, a variation in grain size is observed (see Fig. 4b, -120 V bias), which is due to re-nucleation effects documented by the local FWHM alteration [12], accompanied by an oscillating evolution of the hardness profile. The number of defects, which contributes to hardness in the individual growth stages, results also in high residual stresses [32]. Thus, in the middle section, which is characterized by high H, also high residual stresses can be assumed to be present [12]. In the upper section of the film (-40 V bias), the crystallites grow again with a needle like structure. Grain coarsening as a consequence of columnar growth takes place rapidly with increasing film thickness, which leads to well-developed crystallites (see Fig. 4b, upper section). Again a decrease of the hardness with increasing film thickness is observed, being in agreement with the FWHM plot in Fig. 4a. The hardness measured close to the film surface was determined to be 20.5 GPa. H was found to be lowest in this region, as the grains are well-developed close to the film surface. This is a reasonable value if compared with results gained by conventional nanoindentation of the film surface [21], representing only the hardness of the surface-near zone, not enabling to resolve hardness depth-variations.

Additionally, sudden changes of the microstructure observed at the interfaces between the bottom/middle and the middle/upper section affect the hardness of the film (Fig. 4c). A disruption of the columnar grains is observed at the interface of the bottom/middle section as a consequence of the change in ion bombardment conditions (see Fig. 4c, left). This leads to re-alignment of crystallites, which evolve with small grained V-shaped structure at early grow stages. Also the interface located between the middle and the top section of the film shows a similar effect. Film growth conditions are abruptly changed at this interface - the highly distorted structure develops towards more ordered columnar growth. Besides small crystallites, a large number of defects is expected to be present in these two regions of early stages of thin film growth, immediately after changing the ion bombardment conditions. Thus, even if the thin film represents a single-phase structure, the presence of these adjacent sublayers further contributes to a local increase of H as they are constrained due to different lattice distortion.

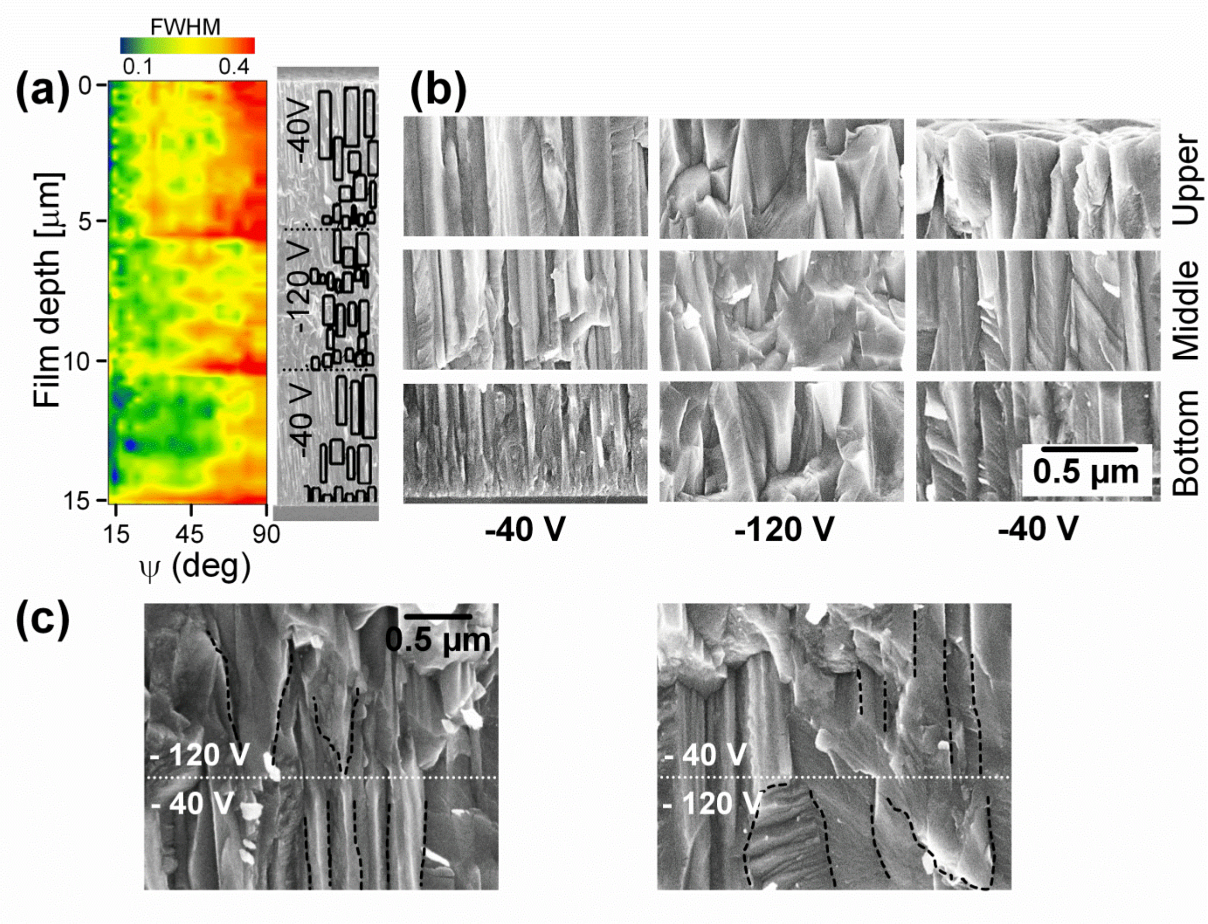

Fig. 4: *(a) Film cross-section with FWHM plot of CrN 111 reflections demonstrating the microstructural evolution in the individual growth stages, (b) SEM micrographs of the three sections of the film revealing the thickness-dependent microstructure in more detail, (c) high-resolution SEM micrographs of the regions where the ion energy has been changed during film growth.*

5. Conclusions

Local properties of hardness and elastic modulus of a sputtered nanocrystalline CrN thin film, prepared with a bias variation ranging from -40 to -120 V, have been investigated by nanoindentation using a depth-profiling technique and microstructure related alterations have been observed. Apparent changes in texture are shown to have almost no effect on the elastic modulus due to the isotropic response of the film during indentation. The local growth conditions, adjusted by the different substrate bias voltage used at different stages of film growth, are identified to mainly determine the hardness due to the resulting variation in grain size and defect density. The hardness for nanocrystalline single-phase CrN is shown to vary between 20.5 GPa, which represent regions with well-developed coarsened grains, and 24.0 GPa at areas characterized by highly distorted small crystals. The observed findings confirm the general notion of a growth-related hardness gradient in single-phase nanocrystalline thin films.

Acknowledgement

Financial support by the Austrian Federal Government (in particular from Bundesministerium für Verkehr, Innovation und Technologie and Bundesministerium für Wirtschaft, Familie und Jugend) represented by Österreichische Forschungsförderungsgesellschaft mbH and the Styrian and the Tyrolean Provincial Government, represented by Steirische Wirtschaftsförderungsgesellschaft mbH and Standortagentur Tirol, within the framework of the COMET Funding Programme is gratefully acknowledged.

References

[1] B. North, Six issues for the hard coatings community, Surf. Coat. Technol. 106 (1998) 129-134.

[2] K. Wetzig, C.M. Schneider, Metal Based Thin Films for Electronics, second ed., Wiley-VCH, Dresden, 2006.

[3] R. Daniel, J. Musil, Novel Nanocomposite Coatings: Advances and Industrial Applications, Pan Stanford Publishing, Singapore, London, New York, 2014.

[4] B.A. Movchan, A.V. Demchishin, Investigation of the structure and properties of thick vacuum deposited films of nickel, Phys. Met. Metallogr. 28 (1969) 653-660.

[5] J.A. Thornton, Influence of apparatus geometry and deposition conditions on the structure and topography of thick sputtered coatings, J. Vac. Sci. Technol. 11 (1974) 666-670.

[6] R. Messier, A.P. Giri, R.A. Roy, Revised Structure Zone Model for Thin Film Physical Structure, J. Vac. Sci. Technol. A 2 (1984) 500-503.

[7] P.B. Barna, M. Adamik, Fundamental structure forming phenomena of polycrystalline films and the structure zone models, Thin Solid Films 317 (1998) 27-33.

[8] I. Petrov, L. Hultman, U. Helmersson, J.E. Sundgren, Microstructure modification of TiN by ion bombardment during reactive sputter deposition, Thin Solid Films 169 (1989) 299-314.

[9] J. Keckes, M. Bartosik, R. Daniel, C. Mitterer, G. Maier, W. Ecker, J. Vila-Comamala, C. David, S. Schoeder, M. Burghammer, X-ray nanodiffraction reveals strain and microstructure evolution in nanocrystalline thin films, Scripta Mater. 67 (2012) 748-751.

[10] H. Dölle, The influence of multiaxial stress states, stress gradients and elastic anisotropy on the evaluation of (Residual) stresses by X-rays, J. Appl. Cryst. 12 (1979) 489-501.

[11] G. Genzel, Evaluation of stress gradients sigma(ij)(z) from their discrete laplace transforms sigma(ij)(tau(k)) obtained by X-ray diffraction performed in the scattered vector mode Phys. Status Solidi A 156 (1996) 353-363.

[12] R. Daniel, J. Keckes, I. Matko, M. Burghammer, C. Mitterer, Origins of microstructure and stress gradients in nanocrystalline thin films: The role of growth parameters and self-organization, Acta Mater. 61 (2013) 6255-6266.

[13] P.H. Mayrhofer, C. Mitterer, H. Clemens, Self-Organized Nanostructures in Hard Ceramic Coatings, Adv. Eng. Mater. 7 (2005) 1071-1082.

[14] S. Ulrich, C. Ziebert, M. Stüber, E. Nold, H. Holleck, M. Göken, E. Schweitzer, P. Schlossmacher, Correlation between constitution, properties and machining performance of TiN/ZrN multilayers, Surf. Coat. Techol. 188-189 (2004) 331-337.

[15] C. Ziebert, C. Bauer, M. Stüber, S. Ulrich, H. Holleck, Characterisation of the interface region in stepwise bias-graded layers of DLC films by a high-resolution depth profiling method, Thin Solid Films 482 (2005) 63-68.

[16] Z.H. Xu, X. Li, Effect of sample tilt on nanoindentation behaviour of materials, Philos. Mag. 87 (2007) 2299-2312.

[17] W.C. Oliver, G.M. Pharr, An improved technique for determining hardness and elastic modulus using load and displacement sensing indentation experiments, J. Mater. Res. 7 (1992) 1564-1583.

[18] C. Riekel, M. Burghammer, R. Davies, Progress in micro- and nano-diffraction at the ESRF ID13 beamline, IOP Conf. Ser. Mater. Sci. Eng. 14 (2010) 012013.

[19] A.P. Hammersley, S.O. Svensson, M. Hanfland, A.N. Fitch, D. Hausermann, Two-dimensional detector software: From real detector to idealised image or two-theta scan High Pressure Res. 14 (2006) 235-248.

[20] M.A. Hopcroft, W.D. Nix, T.W. Kenny, What is the Young's Modulus of Silicon?, J. Microelectromech. S. 19 (2010) 229-238.

[21] H. Ichimura, I. Ando, Mechanical properties of arc-evaporated CrN coatings: Part I - nanoindentation hardness and elastic modulus, Surf. Coat. Technol. 145 (2001) 88-93.

[22] H.-R. Wenk, Eine Gefüge-Röntgenkamera, Schweiz. Min. Petr. Mitt. 43 (1963) 707-719.

[23] F. Heidelbach, C. Riekel, H.-R. Wenk, Quantitative texture analysis of small domains with synchrotron radiation X-rays, J. Appl. Cryst. 32 (1999) 841-849.

[24] G. Knuyt, C. Quaeyhaegens, J. D'Haen, L. Stals, A model for texture evolution in a growing film, Surf. Coat. Technol. 76-77 (1995) 311-315.

[25] J. Almer, U. Lienert, R.L. Peng, C. Schlauer, M. Oden, Strain and texture analysis of coatings using high-energy x-rays, J. Appl. Phys. 94 (2003) 697-702.

[26] J.J. Vlassak, W.D. Nix, Indentation modulus of elastically anisotropic half spaces, Philos. Mag. A 67 (1993) 1045-1056.

[27] H. Ljungcrantz, M. Oden, L. Hultman, J.E. Greene, J.E. Sundgren, Nanoindentation Studies of Single-Crystal (001), (011), and (111) Oriented TiN Layers on MgO, J. Appl. Phys. 80 (1996) 6725-6733.

[28] H. Gleiter, Nanocrystalline Materials, Springer, Berlin, 1991.

[29] E. Arzt, Size effects in materials due to microstructural and dimensional constraints: a comparative review, Acta Mater. 46 (1998) 5611-5626.

[30] H. Gleiter, Nanostructured materials: basic concepts and microstructure, Acta Mater. 48 (2000) 1-29.

[31] H. Oettel, R. Wiedemann, Residual stresses in PVD hard coatings, Surf. Coat. Technol. 76 (1995) 265-273.

[32] F. Vaz, P. Machado, L. Rebouta, J.A. Mendes, S. Lanceros-Mendez, Physical and morphological characterization of reactively magnetron sputtered TiN films, Thin Solid Films 420 (2002) 421-428.

Publication IV

Mechanical Property Enhancement in Laminates through Control of Morphology and Crystal Orientation

A. Zeilinger, R. Daniel, M. Stefenelli, B. Sartory, L. Chitu, M. Burghammer, T. Schöberl, O. Kolednik, J. Keckes, C. Mitterer

Submitted for publication.

Mechanical Property Enhancement in Laminates through Control of Morphology and Crystal Orientation

A. Zeilinger[a], R. Daniel[b], M. Stefenelli[a], B. Sartory[a], L. Chitu[a], M. Burghammer[c],
T. Schöberl[d], O. Kolednik[d], R. Daniel[b] and C. Mitterer[d]

[a] *Materials Center Leoben Forschung GmbH, Roseggerstraße 12, 8700 Leoben, Austria*

[b] *Department of Physical Metallurgy and Materials Testing, Montanuniversität Leoben, Franz-Josef-Straße 18, 8700 Leoben, Austria*

[c] *ESRF, 38043 Grenoble, France*

[d] *Erich Schmid Institute of Materials Science, Austrian Academy of Sciences and Department of Materials Physics, Montanuniversität Leoben, 8700 Leoben, Austria*

Abstract

This article shows the successful implementation of biological design principles into synthetic laminate materials in order to enhance their mechanical properties. We demonstrate and provide a strategy for laminate thin films, which reveals that the control of local crystal anisotropy across laminates together with the optimized layered arrangement are essential for their mechanical behavior. By the example of a laminate consisting of brittle CrN and ductile Cr layers, enhanced material properties are achieved by taking advantage of the self assembly mechanisms of the heterogeneous material during film growth. The usage of local microstructure analysis by a synchrotron based technique as well as miniature mechanical tests allow to understand the relationship between the apparent local microstructure and the accompanied mechanical properties. A crystallographic orientation relationship between Cr and CrN is elucidated, which leads to decisive mechanical enhancement due to microstructural benefits in terms of texture. This results in enhanced strength and fracture toughness of the laminate compared to its single constituents. The systematic approach gives an insight into the complex coherences of laminate materials, where the used techniques and design principles are universally applicable.

Keywords: nanostructure, anisotropy, structure-property relationship, composite material, thin film

1. Introduction

Biological design principles have already found their way into technical applications providing the nucleus for many of the advanced materials we take for granted today. This multitude of ideas has always been highly regarded for design issues by materials scientists independent of their research field, as the available structures in nature typically exhibit a sophisticated hierarchical architecture [1-3]. It serves as the basis for strong and tough materials due to the combination of a broad range of unique and fascinating structural elements at small length scales as present e.g. in seashell, bone or spider silk [4-7].

One remarkable structural feature of biological materials is their periodic lamellar structure, which allows them to withstand external mechanical loads as well as makes them insensitive to flaws at nanoscale [8]. Their mechanical properties are invariably defined by the structural arrangement, which is an inherent material feature of high scientific and technical interest [9].

Thus, in the field of nanostructured engineering materials, the idea of synthesizing laminate materials seems to be promising [10-14], as miniature devices generally have high strength but also exhibit brittle behavior and fail immediately after a crack is initiated. This approach, however, often results in materials with mechanical properties lying magnitudes below those found in nature. This is due to the fact that when copying from nature, the architectural configurations and material characteristics are generally imitated for the synthetic structural components, but not the natural materials themselves. Nature is assembled by elements, which are lightweight and more fragile. For engineering materials typically heavier, bulky and more durable materials are selected, as they have to withstand rough environmental conditions, e.g. wider temperature ranges or mechanical loading and thus require different material selection [14]. The manufacturing-driven simplification in engineering leads to a loss of the complex heterogeneous architecture characteristic for biological materials, which enables a local tuning of the mechanical properties, especially the local elastic modulus, strength and toughness.

This is mainly the reason why biological design strategies are not directly applicable in developing new engineering materials, as there are limitations in the fabrication possibilities [15-17]. As a result, different strategies for their integration have to be pursued to receive the desired functionality and adequate properties of novel materials. Therefore, besides the implementation of a layered architecture, an extensive research has focused on the assembly mechanisms involved in the last years. This should allow tuning of materials by intelligent structuring. However, only a limited number of successful approaches have been reported so far [18-21].

Nanostructured thin film materials have raised enormous interest in the last years as possible candidates for materials to achieve such outstanding properties. As their growth typically takes place far away from thermodynamic equilibrium, these materials often exhibit a heterogeneous nature. This allows the synthesis of a material by maneuvering atom by atom [22], which is seen as a promising pathway in materials development. Nevertheless, the synthesis of bio-inspired materials as a research field has not gained much attention so far, since the characterization of these heterogeneous materials is due to lacking high-resolution techniques a challenging task. Fortunately, our knowledge of these structures has increased significantly in recent years as there is rapid progress in the field of position resolved synchrotron based techniques and micromechanical tests for small scale geometries. The analysis of these materials regarding chemical composition, phase evolution, texture and crystallite size has become possible now. This allows an insight into the complex relationship between synthesis conditions, microstructure and mechanical properties of laminated materials, which is crucial for designing new materials with exceptional performance.

In this work, we demonstrate the ability of laminate materials to withstand severe mechanical demands by controlling their structuring at small scale in a synthetic layered composite material. Cr/CrN laminates, consisting of brittle ceramic CrN and ductile metallic Cr layers, serve as a model system for investigating both, the laminate structure with alternating layered arrangement as well as the single constituents [23-26]. We propose a strategy consisting of a detailed local microstructural analysis of these materials as well as adequate mechanical tests as tools to evaluate and understand the relationship between the apparent microstructure and mechanical properties of such nanostructures. The anisotropic nature of the materials involved is shown to be used effectively in order to generate a laminated composite material with improved strength and resistance against fracture. The dominating effects and mechanisms responsible for the enhanced mechanical properties of the laminates, caused by the controlled material assembly, are revealed in detail. The results show that there is an enormous potential for laminated material systems with exceptional functionalities and durability in mechanically challenging applications.

2. Results and Discussion

Nanostructured thin films exhibit a wide variety of local microstructural features, which control their mechanical properties [27]. These features include phase composition, morphology, crystallographic texture, grain size and structural defects. In order to understand the relationship between the local structure and the resulting mechanical properties, a set of samples consisting of Cr and CrN single layers as well as the corresponding laminate materials with a total thickness of 3 μm were synthesized by plasma-assisted vapor deposition. The individual layer thicknesses of the laminates are $\Lambda_{Cr} = 0.5$ / $\Lambda_{CrN} = 1.0$ μm and $\Lambda_{Cr} = 0.25$ / $\Lambda_{CrN} = 0.5$ μm, named “0.5/1.0-laminate” and “0.25/0.5-laminate” in the following. The elemental composition of CrN was determined by wavelength-dispersive X-ray spectroscopy to be close to stoichiometry (N/Cr =

1 -1.09), the Ar and O content was detected to be below 1 at % depicting a low level of deposition process-related contamination.

2.1. Local microstructure characterization

Cross-sectional scanning electron microscopy (SEM) images in Figure 1 (A-D) illuminate the microstructural evolution of the samples, indicating crystalline growth in all cases. The micrograph in (A) shows metallic Cr growing with fine crystallites, which extend to a columnar coarse grained structure with increasing film thickness. The film structure is dense and the film surface smooth with grains arranged parallel to each other, indicating a fiber textured morphology. Using optimized growth parameters [28], this type of microstructure develops due to high adatom mobility of condensing Cr atoms, resulting in the presented dense structure. The morphology of CrN is depicted in (B) and its structure is characterized by small randomly oriented crystallites formed during the early growth stage, extending to V shaped coarsened crystallites with increasing film thickness. This type of microstructure typically evolves if crystals are overgrown by others due to competitive grain growth [29]. In (C) the 0.5/1.0-laminate is shown, starting with Cr at the bottom. Although the layers appear to be separated by the individual interfaces, the SEM micrograph of the focused ion beam (FIB) polished fracture surface illuminates sharp interfaces between the individual Cr and CrN layers and continuous crystal growth along the whole film thickness, resulting in fully developed grains. The morphology of the laminate film is also columnar, but the crystallite size is slightly reduced compared to single layered CrN. The decrease of the thickness of Cr and CrN layers to 0.25 and 0.5 µm, respectively, promotes crystal refinement, as illustrated in (D). A low magnification transmission electron microscopy (TEM) image in (E) provides insight into the laminate structure and reveals a column on column alignment at the Cr/CrN interface [28]. A detailed bright-field image analysis reveals the presence of a ~10 nm thick transition layer, identified to be hexagonal Cr_2N as reported by Zhang et al [30]. However, this transition layer does not affect the columnar microstructure. TEM reveals a well-defined and sharp interface formed between Cr and Cr_2N (F), whereas the atomic planes between the Cr_2N and CrN grains interpenetrate and the interface appears blurred as evidenced by the low image contrast (E).

The local characterization of microstructure is of vital importance in order to establish structure property relationships for layered materials. However, the material structure at the nanoscale was hardly accessible up to now, since the necessary information and/or required resolution could not be provided by the available techniques like X-ray diffraction, TEM or atom probe tomography. However, recently the development of advanced synchrotron sources has made rapid progress and led to the development of small X-ray beam sizes with diameters below 100 nm, offering new perspectives for material characterization [31]. This technique has been recently adapted to characterize nanostructured materials [32], enabling position resolved determination of phase composition, crystallographic texture, crystallite size and strain.

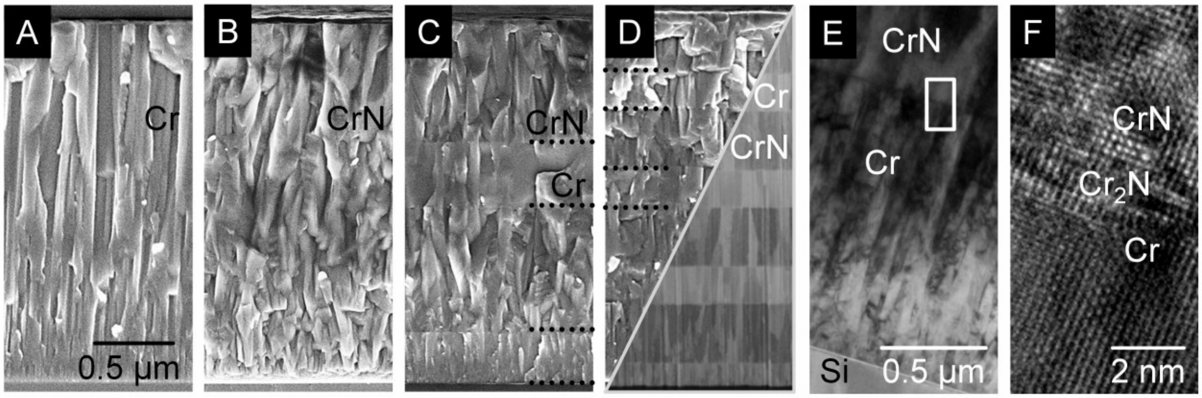

Fig. 1.: *SEM cross-sectional micrographs of nanostructured single-layered (A) Cr and (B) CrN, (C) 0.5/1.0-laminate and (D) 0.25-0.5-laminate. FIB polishing reveals the heterogeneous nature of the laminate material throughout the entire thickness. The overall thickness was maintained constant at 3 µm and the growth direction is from bottom to top. The dotted lines indicate the interfaces between Cr and CrN layers. A low magnification bright-field TEM image (E) illustrates the CrN Cr interface and the evolution of columnar grains. (F) The HR-TEM image illuminates the formation of an interfacial Cr2N transition layer with a thickness of ~10 nm between Cr and CrN.*

Figure 2 illustrates the normalized X-ray diffraction intensity distribution depth profiles of the single-layer and laminate materials as a function of their 2θ diffraction angles. The data were obtained by 2θ integration of the Debye-Scherrer rings in the range of 0 to 360 degrees, which were collected in 100 nm steps across the film thickness. The phase evolution of metallic Cr is illustrated in (A), revealing growth towards a polycrystalline structure with 110 and 100 oriented grains. The strong texture is a typical phenomenon of metallic films, where low-energy surfaces exhibit high adatom mobility [33]. This preferred growth is already present at low temperatures. The 100 texture is dominating already during the early growth stage, revealing the Cr layer to be strongly oriented. The diffraction data depicted in (B) reveal single-phase face-centered cubic (fcc) CrN, forming polycrystalline grains oriented in 111, 100 and 110 direction along the film thickness. The 111 and 200 peaks are the dominant contributions of the CrN layer. While (100) and (111) oriented grains coexist at the early growth stage, the (111) orientation dominates at greater thicknesses. The pronounced (111) texture has also been reported for other fcc transition-metal nitrides [34-35]. The combination of Cr and CrN layers in the arrangement of a layered laminate has a significant effect on the texture development as evidenced by the micrograph in (C). CrN is forced to change its texture from 111 into predominately 100 oriented grains when grown on a Cr layer, since the predominant 111 orientation of CrN is suppressed as the film grows on a Cr surface with strong 100 orientation. Choosing suitable kinetic and thermal activation for film growth [28], Cr acts as an epitaxial template for CrN, due to the small lattice misfit ($d_{Cr}(100) = 2.88$ Å and $d_{CrN}(110) = 2.93$ Å) of the bcc Cr (100) and fcc CrN (100) planes [36]. The observations are in accordance with the SEM micrographs in Figure 1 (C), which reveal the CrN layers to change their appearance towards a fiber texture. A decrease of the Cr and CrN layer thicknesses, as shown in (D), leads to an even more pronounced texture change of CrN towards 100. This is illustrated by the low intensity of the 111 and the increase in intensity of the 200 peak. Summarizing, it is evident that nanostructured layers synthesized by vapor deposition can be structurally tailored at the atomic scale. This can be achieved by controlling their growth orientation using suitable growth conditions as well as crystallographic templates.

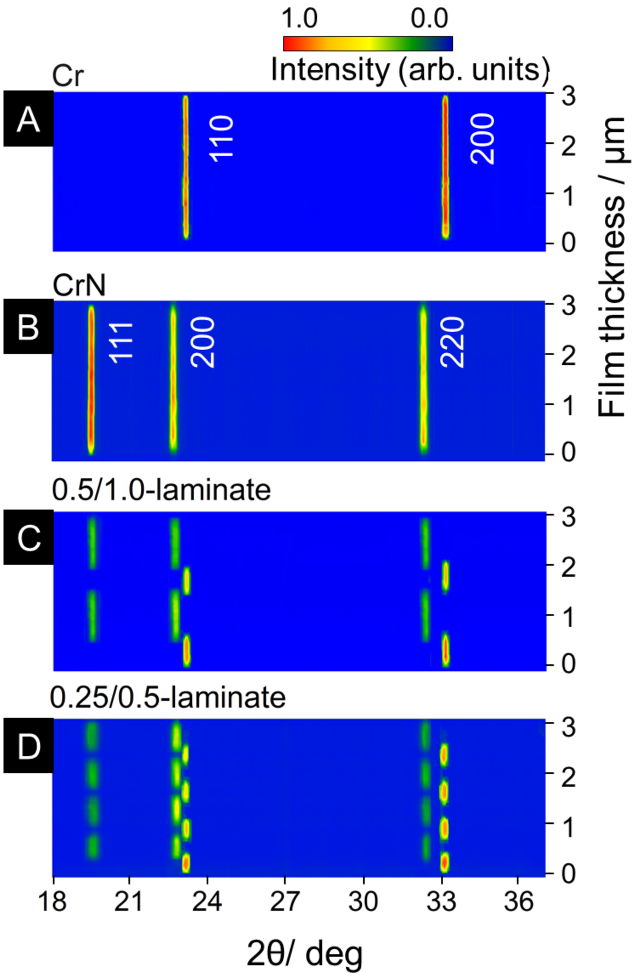

Fig. 2.: *Local microstructure analysis by cross-sectional scanning X-ray nanodiffraction. The scans reveal the intensity distribution of Cr 110 and 200 and CrN 111, 200 and 220 reflections. (A) Cr and (B) CrN as well as the (C) 0.5/1.0-laminate and (D) 0.25/0.5-laminate were scanned along their cross-section using a step size of 100 nm. The data were extracted from Debye-Scherrer rings recorded at different positions across the film thickness. Crystallographic texture is shown to vary significantly as indicated by the different intensity distributions.*

2.2. Micromechanical characterization

It is obviously tempting to study the effect of the observed differences in microstructure of the single-layered and the laminate samples on their mechanical properties.

Micromechanical test specimens were prepared using a FIB technique, carefully avoiding damage during preparation [37-38]. Prior to FIB milling, the Si wafer used for growth of the film samples was removed. Micron-sized fracture-mechanical samples having the geometry of bending beams as shown in Figure 3 (A) were fabricated. The bottom-view in (B) confirms the preservation of the complete structure of the films, i.e. including the nanograins at the interfacial area as well as the fully developed columnar structure at greater film thickness. Subsequently, the beams have been loaded by the diamond tip of a nanoindentation system until film fracture. The fracture stress was determined at the maximum load applied to unnotched beams when fracture occurs.

Figure 3 (C) depicts the load-deflection curves of all samples. The single-layer Cr behaves purely elastic over a wide load range, as shown by the constant slope. For high loads applied, the load-displacement ratio decreases, which indicates plastic deformation. Fracture of the specimen occurs at the abrupt end of the curve. In contrast, CrN exhibits a fully linear-elastic curve until fracture, which indicates brittle material behavior. The load deflection curves of both Cr/CrN laminates exhibit a small non-linearity as visible in the plot. As the load deflection characteristics are derived from bending beams of similar size, one can easily identify the laminate with the smallest layer thicknesses as the mechanically stiffest and therefore strongest of the samples investigated. This may be surprising at first glance, as the laminates consist of brittle and ductile layers. Nevertheless, these significantly enhanced mechanical properties can be explained by taking into account the microstructural features determined by X-ray nanodiffraction. The measurements revealed a strong change from a (111) towards (100) texture for CrN grown on a Cr layer. Considering the elastic constants for Cr and CrN, c44 = 88, c12 = 59 and c44 = 99 GPa for Cr and c11 = 340, c11 = 542, c12 = 27 GPa for CrN, it is seen that both materials are stiffest along the <100> and softest along the <111> orientation [39-40]. Since the laminate architecture exhibits, as shown in Figure 2, a well-developed 100 texture for both Cr and CrN layers, a higher stiffness can be assumed, as also confirmed by the experiment.

The experimental setup used allows not only identification of the stiffest material, but also enables the determination of the orientation-dependent elastic modulus of the samples. The values of the elastic modulus were determined from the slope of the load-deflection curves to be 162 ± 9 GPa for Cr, 269 ± 12 GPa for CrN and 274 ± 8 and 323 ± 16 GPa for the 0.5/1.0-laminate and 0.25/0.5-laminate, respectively. If the rule of mixture is taken into account, the values for the single layers as well as laminates correspond well to the elastic constants given above. Nevertheless, the values of the single layers are lower than those calculated from the single elastic constants of both materials. This difference is attributed to differences in the microstructure, where the values given in literature consider a perfect single crystal. However, in our experiment crystal growth leads to the formation of grain boundaries and point defects, which decrease the elastic modulus of the film. In addition to the modulus, also the fracture stress [32] can be calculated from the load-displacement curves, revealing the laminate with the highest stiffness also to exhibit the highest fracture stress σ_{max} = 7.81 ± 0.3 GPa, compared to the 0.5/1.0-laminate laminate (σ_{max} = 6.21 ± 0.2 GPa) and the single layers CrN (σ_{max} = 5.76 ± 0.2 GPa) and Cr (σ_{max} = 4.77 ± 0.1 GPa). Thus, we can conclude that the laminates consisting of ductile Cr and brittle CrN have improved stiffness and fracture stress by taking advantage of the materials anisotropy.

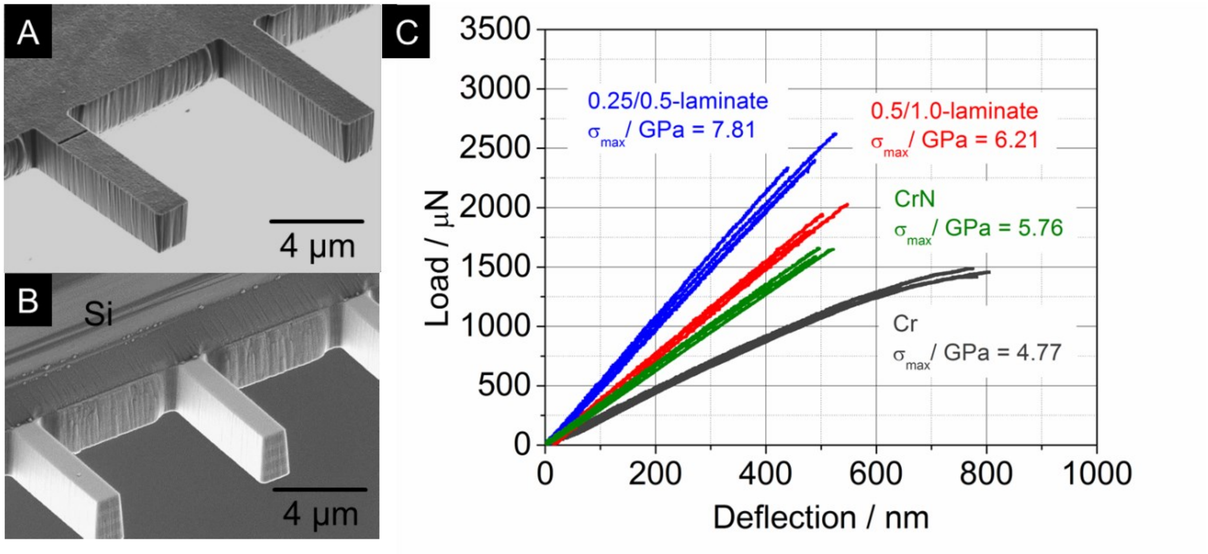

Fig. 3.: Micromechanical characterization using specimens having a bending beam geometry. SEM micrographs depict (A) the top-view of single-layered Cr with unnotched and notched beams. (B) Bottom-view of a FIB shaped 0.25/0.5-laminate. Before testing of the bending beams the Si wafer was removed. (C) Load-deflection curves of the

unnotched samples depicting the 0.25/0.5-laminate to exhibit the highest fracture stress. The end of the curves indicates fracture.

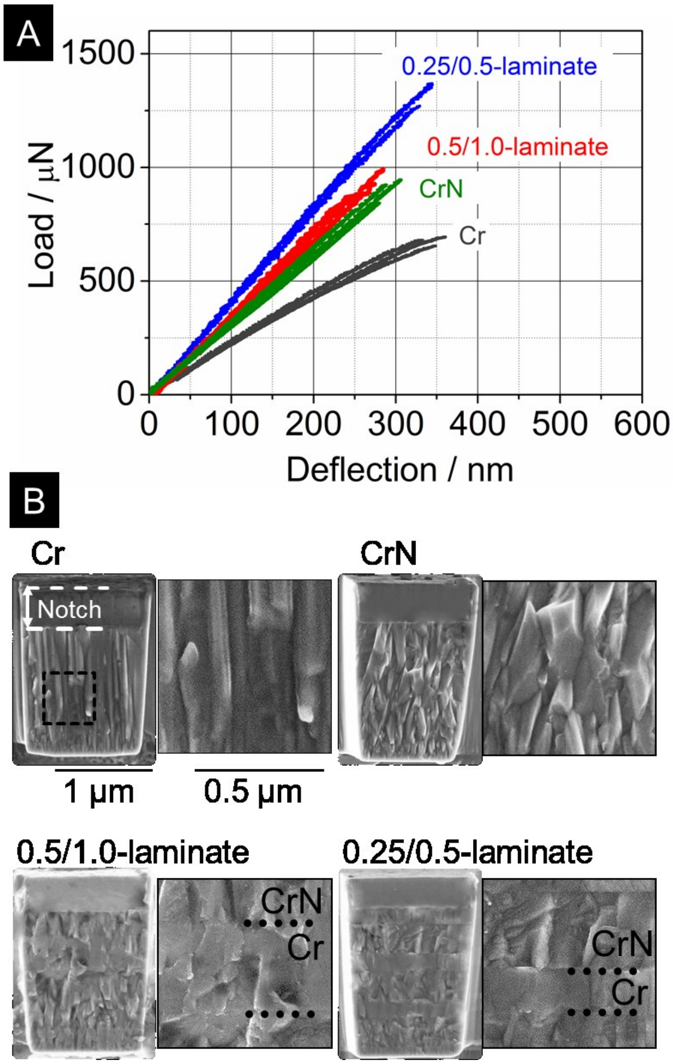

Fig. 4.: *Bending tests with notched beams provide information on the resistance of the samples against crack propagation. (A) Load-deflection curves for the different samples depicting the 0.25/0.50- laminate to withstand the highest load. (B) SEM micrographs of the fracture surfaces and their high-resolution details reveal different fracture morphologies.*

The resistance of our samples against propagation of cracks, i.e. fracture toughness, was determined by the same type of experiment. In order to imitate a pre-existing crack, a fine notch with a depth of 500 nm has been introduced to the samples. The samples failed at lower load compared to the unnotched specimens, as depicted in Figure 4 (A). The curve shape for all samples is similar to those of the bending experiment of unnotched specimens. Interestingly, no improvement of the fracture toughness of the 0.5/1.0-laminate with respect to the CrN single-layer is observed (K_{IC}-Cr = 2.40 ± 0.2 $MPam^{1/2}$, K_{IC}-CrN = 3.10 ± 0.2 $MPam^{1/2}$, K_{IC}-0.5/1.0-laminate = 3.25 ± 0.2 $MPam^{1/2}$). This is in contrast to the 0.25/0.5-laminate, exhibiting the highest fracture load of all samples with K_{IC} = 4.35 ± 0.2 $MPam^{1/2}$. A detailed analysis of the load-deflection curve indicates that crack propagation of this sample was found to be interrupted several times during loading. The areas of sudden crack propagation and arrestment, which go along with kinks in the load-deflection data and a subsequent decrease of the slope of the curve, are small but they indicate that the laminate fails in a step-wise manner.

In order to gain insight into the fracture behavior of the samples, the fracture surfaces were studied by SEM, as shown in Figure 4 (B). The fracture surface of the single-layer Cr allows to clearly identify the columnar structure of the film (compare Figure 1 (A)), indicating plastic deformation of the individual columns (see the high-resolution SEM micrograph in Figure 4 (B)). In contrast, the single-layer CrN is characterized by macroscopically brittle fracture with very limited plasticity, corresponding to the brittle nature of the material. These observations are in good agreement with the load-deflection curves of both single-layered materials (see Figure 4 (A)). The fracture surface of the 0.5/1.0-laminate appears very smooth; however, the alternating Cr and CrN layers are still visible. While the fracture surface of the CrN layer again indicates brittle behavior, the Cr surface appears partly blurred and deformed. This effect is even more pronounced for the 0.25/0.5-laminate.

In order to obtain a more detailed insight into the fracture mechanisms of the laminate, high resolution atomic force microscopy (AFM) investigations have been carried out for the 0.25/0.5-laminate. A lamellae containing the full fracture surface, as shown in Figure 5 (A), was cut off from the fractured sample using the FIB and transferred and fixed horizontally aligned onto a Si sample holder. The individual Cr and CrN layers of the sample are clearly visible in the SEM image in (A) and can be distinguished as Cr appears brighter. Crack propagation occurred from the right to the left; the notch introduced by the FIB is visible. The fracture surface (see Figure 1) is undulated as indicated by the varying sample height along the film thickness. AFM line profiles have been recorded along the crack propagation direction in order to obtain a detailed view of the surface height profile. Two profiles, revealing the waviness of the sample along its film thickness, are depicted in (B). The profile exhibits local minima as well as maxima at the interfaces between the individual layers, indicating that the propagating crack is deflected at the interfaces, preventing the Cr/CrN laminate from early failure. Furthermore, AFM phase contrast mode has been used as shown in (C) to investigate local differences in fracture behavior and the interface of the laminate. This mode provides more information of fine features, such as grain boundaries or interfaces, which can be obscured by the rough topography. The columnar structure of the CrN layer is shown to be retained after fracture, a sharp-edged topography can be found, indicating the layer to fail along its grain boundaries. On the contrary, the Cr layer appears to be very smooth and grain boundaries no longer visible. This suggests that transcrystalline fracture contributes to the failure of the Cr layer in the laminate. This is in contrast to the Cr single layer, where fracture has been identified to be intercrystalline.

The observation of crack deflection at the interfaces of the 0.25/0.5-laminate is an interesting feature, as these materials consist only of crystalline components compared to biological structures, which typically exhibit an alternating crystalline-amorphous architecture. The effect is fundamentally different from the crack inhibition concepts given by nature, but not undiscovered in materials science. There has been extensive work by Fratzl et al. and Kolednik et al. [10-13], who already predicted that an inhomogeneous material, which exhibits a spatial variation in the elastic modulus, can have a much higher apparent resistance against fracture and crack propagation than a comparable homogeneous material. By simple fracture mechanical considerations they have shown that this effect occurs due to a strong decrease of the crack driving force, which leads to crack arrest [13]. There are several other effects which may contribute to the enhanced material behavior of the 0.25/0.50-laminate material. On the one hand, the fracture surface of this laminate was found to be undulated, which indicates increased energy required for forming the fracture surface. The contribution of this effect to the enhancement of the material properties is assumed to be a minor one, as the deflection angle is small. Much more effective might be the change in the failure mechanism from intercrystalline into transcrystalline fracture of the Cr layers, which is observed with decreasing layer thickness. Since the specific fracture surface energy for transcrystalline fracture is, in general, higher than that of intercrystalline fracture, this will improve the crack growth resistance of the laminate. In addition, the effect of possible intrinsic growth stresses on the materials behavior are to be mentioned. By this experiment the predictions on increased fracture stress and fracture resistance in inhomogeneous materials with decreased layer thickness have been confirmed to be valid even at small scale. This allows promising future prospects for applications of thin laminated materials.

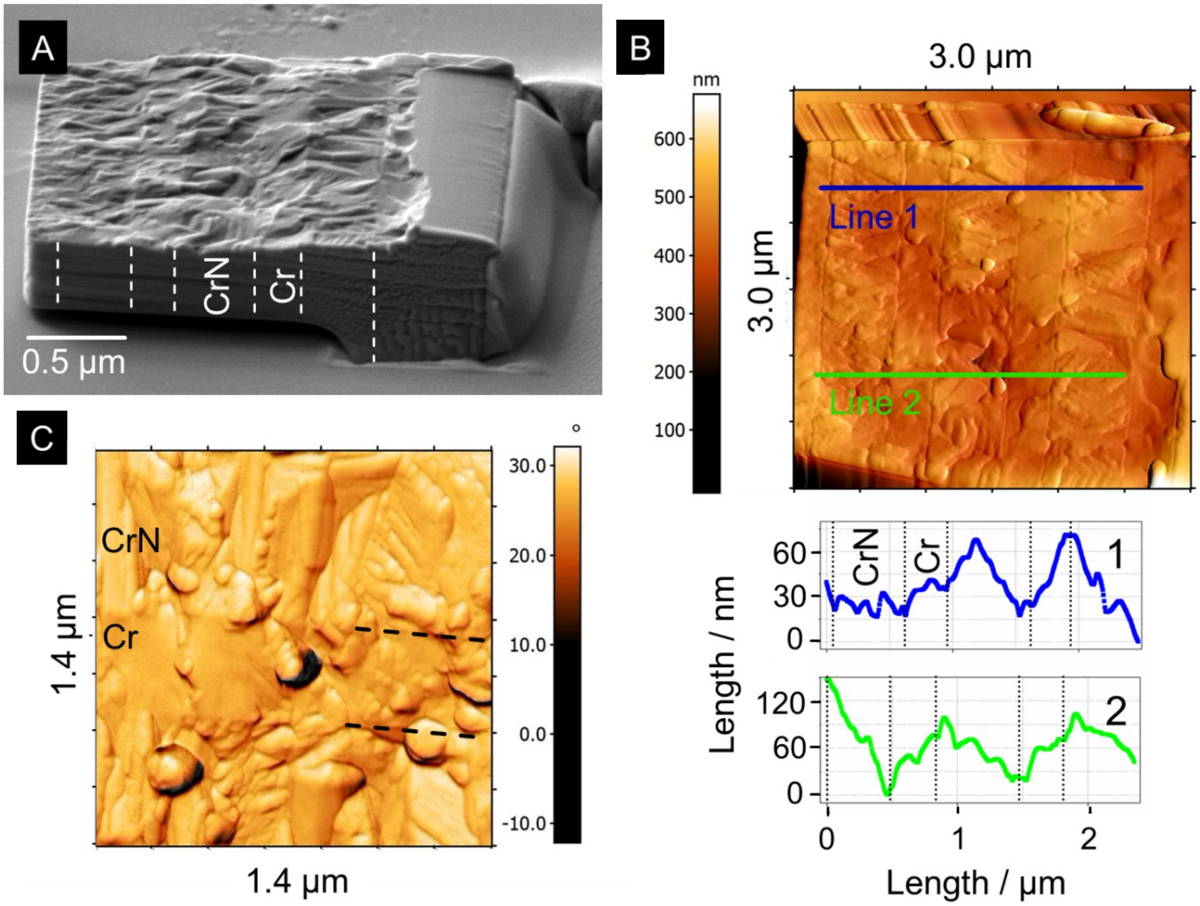

Fig. 5.: *Fracture surface lamellae (A) imaged by SEM of the 0.25/0.5-laminate exhibiting enhanced resistance against crack propagation. For AFM analysis, the lamellae has*

been transferred and fixed onto a Si substrate. (B) AFM topography image and line profiles from different areas of the fracture surface giving indication for crack deflection at the interfaces of the laminate. (C) High-resolution AFM phase image of the sample depicting the CrN/Cr and Cr/CrN interfaces.

3. Summary

Biological materials exhibit unique control over their local composition and orientation of their structural elements at multiple length scales, which enables them to best respond to their environment. In this article, laminated thin film materials have been shown to be potential candidates for the integration of these bio-inspired design principles, as their heterogeneous nature provides the basis for the synthesis of materials with outstanding mechanical properties. Layered composite architectures, consisting of brittle ceramic CrN as well as ductile metallic Cr forming a laminate, have been synthesized and evaluated by local microstructure characterization and micromechanical tests. Provided that the thickness of the individual layers is small enough, the laminates exhibit considerably improved stiffness, fracture strength and fracture toughness compared to the single layers. Microstructural benefits due to the laminate arrangement as well as orientation relationships between the individual layers are revealed, which can be effectively controlled during film growth. Furthermore, the experiment shows that an amorphous-crystalline structure, as suggested by nature, is not essential in order to implement bio-inspired layered design principles into synthetic materials. This makes nanocrystalline laminates with optimized microstructure interesting for a broad range of future applications due to wide possibilities in materials selection and choice of layer thicknesses.

4. Experimental Section

Sample synthesis: Cr and CrN single-layers as well as Cr/CrN laminate materials consisting of alternating Cr and CrN layers were prepared by reactive unbalanced d.c.

magnetron sputtering (Rapid Coating System, Oerlikon Balzers) from a Cr target produced by powder metallurgy (99.99 % purity, diameter 145 mm, Plansee Composite Materials) [28]. The materials were synthesized in static mode on chemically pre-cleaned Si (100) wafers with the dimensions 20 × 7 × 0.3 mm mounted on a stainless steel sample holder located 20 cm from the target. While the chamber was evacuated to a base pressure of less than 5×10^{-4} Pa, the wafers were heated to 350 °C and subsequently sputter-etched prior to deposition in an Ar plasma for 20 min to remove the native surface oxide layer. The layered materials were then synthesized at a constant total pressure of 1 Pa in an Ar + N_2 gas mixture with a nitrogen partial pressure of 0.25 Pa, a target power of 6 kW and a substrate temperature of 350 °C. The microstructure of Cr and CrN was controlled by the energy of the incident ions using substrate bias voltages of 40 and -80 V, respectively. The laminate materials were prepared without interrupting growth between the individual layers and maintaining a total thickness of 3 µm. Two laminate structures with layer thicknesses of $\Lambda_{Cr} = 0.5$ / $\Lambda_{CrN} = 1.0$ µm and $\Lambda_{Cr} = 0.25$ / $\Lambda_{CrN} = 0.5$ µm were synthesized.

Microstructural characterization: The microstructure of the samples was investigated by a Zeiss Auriga 60 Crossbeam field emission gun scanning electron microscope and a JEOL 2100 F transmission electron microscope, equipped with an image-side Cs-corrector and operated at 200 keV. The FIB milled cross-section, the sample for TEM and the bending beams for micromechanical testing were prepared using an Orsay Physics Cobra Z-05 FIB apparatus. The elemental composition was determined by wavelength-dispersive X-ray spectroscopy using a JEOL JXA840 SEM under an acceleration voltage of 10 kV. A detailed microstructural analysis of phases and texture was performed at the nanofocus extension of the ID 13 beamline at ESRF in Grenoble, France [31]. The experiment was performed in transmission mode using a monochromatic beam at a photon energy of 14.9 keV, being focused to 100 nm in diameter by Kirkpatrick-Baez mirrors. The sample was positioned with the film/wafer interface oriented parallel to the beam and diffraction images were recorded using a CCD area detector with a resolution of 2048 × 2048 pixels. To scan the film cross section, the sample was translated in the beam along its film thickness in 100 nm steps with a typical exposure time of 0.5 s. The two-dimensional diffraction data was processed using the software package Fit2D [41]. In order to ensure comparability of the data with the subsequently performed micromechanical experiments, the synchrotron measurements have been performed in a slice area, where the Si wafer material has been removed. Thus, a possible influence of the thermal mismatch between the films and the Si wafer is avoided. The phase evolution was obtained from integrated intensities of the recorded diffraction patterns along the azimuthal angle of the Debye-Scherrer ring at several measurement points across the film thickness [32].

Micromechanical testing: In order to evaluate the mechanical properties of the samples, micromechanical tests have been performed [37-38]. The films were partially isolated from the Si wafers and, subsequently, bending beams were fabricated using FIB with lengths of 10 µm and widths of 2 µm, where the height corresponds to the film thickness of 3 µm. In order to probe the elastic properties as well as the resistance against crack propagation and fracture, two sets of beams were prepared – the first set without a notch and the second exhibiting a sharp notch with a depth of 500 nm located 2 µm from the wafer support [38]. The beams were subsequently loaded with a spheroconical indenter (tip radius 850 nm) in a nanoindentation system (Hysitron Triboscope), attached to an atomic force microscope (AFM, Digital Instruments 3100). The loading rate has been set to 250 µN s-1. The elastic modulus has been calculated from the slope of the load-deflection curves by taking into account the geometry of the bending beams [42]. The fracture resistance was calculated as the maximum applied load until fracture under consideration of the bending beam dimensions. The fracture toughness was determined from bending experiments using the notched samples, by loading them until fracture and applying linear-elastic fracture mechanics. The surface morphology of the fractured samples was examined in detail by AFM (scanning probe microscope, BRR, DME Company) operating in tapping mode over an area of 3 × 3 µm^2. Measurements of topography and phase-contrast were carried out at ambient temperature using a Si cantilever (NCHR – Point Probe) at a resonance frequency of 320 kHz and a tip curvature radius of 7 nm.

References

[1] G. Jeronimidis, A.G. Atkins, J. Mech. Eng. Sci. 1995, 209, 221.

[2] J.D. Currey, Science 2005, 309, 253.

[3] R. Lakes, Nature 1993, 361, 511.

[4] J.Y. Rho, L. Kuhn-Spearing, P. Zioupos, Med. Eng. Phys. 1998, 20, 92.

[5] S. Kamat, X. Su, R. Ballarini, A.H. Heuer, Nature 2000, 405, 1036.

[6] F. Vollrath, D.P. Knight, Nature 2001, 410, 541.

[7] J. Aizenberg, J.C. Weaver, M.S. Thanawala, V.C. Sundar, D.E. Morse, P. Fratzl, Science 2005, 309, 275.

[8] H. Gao, J. Baohua, I.L. Jaeger, E. Arzt, P. Fratzl, Proc. Natl. Acad. Sci. 2003, 100, 5597.

[9] M.A. Meyers, P.-Y. Chen, A.Y. Lin, Y. Seki, Progr. Mater. Sci. 2008, 53, 1.

[10] P. Fratzl, H.S. Gupta, F.D. Fischer, O. Kolednik, Adv. Mater. 2007, 19, 2657.

[11] O. Kolednik, J. Predan, F.D. Fischer, Eng. Fract. Mech. 2010, 77, 3611.

[12] O. Kolednik, J. Predan, F.D. Fischer, P. Fratzl, Adv. Funct. Mater. 2011, 21, 3634.

[13] O. Kolednik, J. Predan, F.D. Fischer, P. Fratzl, Acta Mater. 2014, 68, 279.

[14] P. Fratzl, J. R. Soc. Interface 2007, 15, 637.

[15] G. Mayer, Science 2005, 310, 1144.

[16] A.R. Studart, Adv. Mater. 2013, 23, 4423.

[17] M.F. Ashby, Materials selection in mechanical design, Butterworth-Heinemann, Oxford, UK 2005.

[18] E. Munch, M.E. Launey, D.H. Alsern, E. Saiz, A.P. Tomsia, R.O. Ritchie, Science 2008, 322, 1516.

[19] P. Podsiadlo, A.K. Kaushik, E.M Arruda, A.M. Waas, B.S. Shim, J.D. Xu, H. Nandivada, B.G. Pumplin, J. Lahann, A. Ramamoorthy, N.A. Kotov, Science 2007, 318, 80.

[20] R.T. Olsson, M. Samir, G. Salazar-Alvarez, L. Belova, V. Strom, L.A. Berglund, O. Ikkala, J. Nogues, U.W. Gedde, Nat. Nanotechnol. 2010, 5, 584.

[21] R.M. Erb, R. Libanori, N. Rothfuchs, A.R. Studart, Science 2012, 335, 199.

[22] R. Feynman, Engineering and Science 1960, 23 (5), 22.

[23] M. Berger, U. Wiklund, M. Eriksson, H. Engqvist, S. Jacobson, Surf. Coat. Technol. 1999, 116-119, 1138.

[24] A. Lousa, J. Romero, E. Martinez, J. Esteve, F. Montala, L. Carreras, Surf. Coat. Technol. 2001, 146 147, 268.

[25] R. Bayon, A. Igartua, X. Fernandez, R. Martinez, R.J. Rodriguez, J.A. Garcia, A. de Frutos, M.A. Arenas, J. de Damborenea, Tribol. Int. 2009, 42, 591.

[26] P. Wiecinski, J. Smolik, H. Garbacz, K.J. Kurzydlowski, Surf. Coat. Technol. 2014, 240, 23.

[27] P.H. Mayrhofer, C. Mitterer, L. Hultman, H. Clemens, Prog. Mater. Sci. 2006, 51, 1032.

[28] R. Daniel, K.J. Martinschitz, J. Keckes, C. Mitterer, J. Phys. D: Appl. Phys. 2009, 42, 075401.

[29] G. Knuyt, C. Quaeyhaegens, J. D´Haen, L.M. Stals, Surf. Coat. Technol. 1995, 76-77, 311.

[30] Z. Zhang, R. Daniel, C. Mitterer, J. Appl. Phys. 2011, 110, 043524.

[31] C. Riekel, M. Burghammer, R. Davies, IOP Conf. Ser.: Mat. Sci. Eng. 2010, 14, 012013.

[32] J. Keckes, M. Bartosik, R. Daniel, C. Mitterer, G. Maier, W. Ecker, J. Vila-Comamala, C. David, S. Schoeder, M. Burghammer, Scripta Mater. 2012, 67, 748.

[33] P.B. Barna, M. Adamik, Growth mechanisms of polycrystalline thin films. In: F.C. Matacotta, G. Ottaviani, editors. Science and Technology of Thin Films. World Scientific publishing Co., Singapore 1995.

[34] W. Ensinger, Nucl. Instrum. Methods: Phys. Res. B 1997, 127-128, 796.

[35] L. Hultman, J.-E. Sundgren, J.E. Greene, D.B. Bergstrom, I. Petrov, J. Appl. Phys. 1995, 78, 5395.

[36] R.Daniel, K.J. Martinschitz, J. Keckes, C. Mitterer, Acta Mater. 2010, 58, 2621.

[37] T.P. Weihs, S. Hong, J.C. Bravman, W.D. Nix, J. Mater. Res. 1988, 3, 931.

[38] A. Riedl, R. Daniel, M. Stefenelli, T. Schöberl, O. Kolednik, C. Mitterer, J. Keckes, Scripta Mater. 2012, 67, 708.

[39] L.B. Freund, S. Suresh, Thin Film Materials: Stress, Defect Formation and Surface Evolution, Cambridge University Press, Cambridge, UK 2003.

[40] J. Almer, U. Lienert, R.L. Peng, C. Schlauer, M. Oden, J. Appl. Phys. 2003, 94, 697.

[41] A.P. Hammersley, S.O. Svensson, M. Hanfland, A.N. Fitch, D. Häusermann, High Pressure Res. 2006, 14, 235.

[42] T.H. Courtney, Mechanical Behavior of Materials, McGraw-Hill, Boston, USA 2000.

Acknowledgements

Dr. Zaoli Zhang is acknowledged for low and high resolution TEM images. Financial support by the Austrian Federal Government (in particular from Bundesministerium für

Verkehr, Innovation und Technologie and Bundesministerium für Wirtschaft, Familie und Jugend) represented by Österreichische Forschungsförderungsgesellschaft mbH and the Styrian and the Tyrolean Provincial Government, represented by Steirische Wirtschaftsförderungsgesellschaft mbH and Standortagentur Tirol, within the framework of the COMET Funding Programme is gratefully acknowledged.